Nature Communications

https://doi.org/10.1038/s41467-026-71189-2

Article in Press

Targeting REV-ERBα/BNIP3 axis attenuates pulmonary arterial hypertension by repressing mitophagy in mice

Received: 7 May 2025

Accepted: 16 March 2026

Cite this article as: Qiu, L., Lu, T., Zhang, J. *et al.* Targeting REV-ERBα/BNIP3 axis attenuates pulmonary arterial hypertension by repressing mitophagy in mice. *Nat Commun* (2026). https://doi.org/10.1038/s41467-026-71189-2

Lejia Qiu, Tingting Lu, Jiayang Zhang, Min Liu, Hui Wang, Wenyu Li, Changxiao Ma, Shuyao Li, Baoyin Ren, Qiong Wang, Fenling Fan, Hu Xu, Feng Zheng, Youfei Guan, Xiaoyan Zhang, Guangrui Yang & Lihong Chen

Manuscript

Targeting REV-ERBα/BNIP3 axis attenuates pulmonary arterial hypertension by repressing mitophagy in mice

Lejia Qiu[1], Tingting Lu[1], Jiayang Zhang[2], Min Liu[3], Hui Wang[3], Wenyu Li[1], Changxiao Ma[1], Shuyao Li[1], Baoyin Ren[1], Qiong Wang[1], Fenling Fan[4], Hu Xu[1], Feng Zheng[1], Youfei Guan[3], Xiaoyan Zhang[1], Guangrui Yang[2*], Lihong Chen[1*]

[1]WuHu Hospital & Health Science Center, East China Normal University, Shanghai, China.
[2]College of Basic Medical Sciences, Shanghai University of Medicine and Health Sciences, Shanghai, China.
[3]Advanced Institute for Medical Sciences, Dalian Medical University, Dalian, China.
[4]Department of Cardiovascular Medicine, First Affiliated Hospital, Xi'an Jiaotong University, Xi'an, Shaanxi, China.

***Correspondence:**
Dr. Lihong Chen
E-mail: lhchen@hsc.ecnu.edu.cn
Address: Health Science Center, East China Normal University, Shanghai 200241, China.
Or
Dr. Guangrui Yang
E-mail: yanggr@sumhs.edu.cn
Address: College of Basic Medical Sciences, Shanghai University of Medicine and Health Sciences, Shanghai 200241, China.

Keywords: Pulmonary arterial hypertension, PASMC proliferation, REV-ERBα, BNIP3, Mitophagy, Mitochondria homeostasis.

Abstract: Pulmonary arterial hypertension (PAH) is a life-threatening metabolic disorder. Nuclear receptors REV-ERBα and REV-ERBβ are established regulators of circadian rhythm and metabolic homeostasis, however their roles in PAH remain unclear. Using *Rev-erbα*$^{+/-}$, VSMC-specific *Rev-erbα*$^{-/-}$, and *Rev-erbβ*$^{-/-}$ mice (only male mice were used in the study), along with pharmacological activation and AAV-mediated overexpression, we found that *Rev-erbα* deficiency, particularly in vascular smooth muscle cells (VSMCs), exacerbates Su5416+hypoxia (SuHx)-induced PAH, whereas Rev-erbα activation or overexpression alleviates disease. In contrast, *Rev-erbβ* loss does not affect PAH. Notably, late-stage administration of REV-ERBα agonist significantly improves established PAH. Mechanistically, REV-ERBα directly represses

Bnip3 transcription, thereby inhibiting BNIP3-driven mitophagy and improving mitochondrial function in hypoxic pulmonary artery smooth muscle cells (PASMCs). *Bnip3* knockdown phenocopies REV-ERBα activation, while *Bnip3* overexpression abrogates REV-ERBα's anti-proliferative effects and accelerates PAH. Collectively, REV-ERBα protects against PAH by inhibiting BNIP3-driven mitophagy and preserving mitochondrial homeostasis in PASMCs. Targeting the REV-ERBα-BNIP3 axis holds promise as a circadian-based therapeutic strategy for PAH.

Introduction

Pulmonary arterial hypertension (PAH) is a progressive and life-threatening disease characterized by the remodeling of pulmonary vasculature, primarily affecting the small pulmonary arteries. This remodeling increases pulmonary vascular resistance, eventually leading to right ventricular (RV) failure[1,2]. Key underlying mechanisms include hyper-constriction of the hypoxic pulmonary vessels and abnormal proliferation of vascular cells, particularly pulmonary artery smooth muscle cells (PASMCs) in the middle layer of the vessel wall[1]. Current therapeutic strategies primarily focus on prostacyclin, endothelin, and nitric oxide pathways, offering symptomatic relief by promoting vasodilation[3]. Despite these advancements, PAH continues to be a life-threatening condition, underscoring the urgent need for innovative therapies that can inhibit PASMCs proliferation, reverse pulmonary vascular remodeling, and improve patient outcomes.

REV-ERBs, including REV-ERBα (also known as NR1D1) and REV-ERBβ (also known as NR1D2), are members of the nuclear receptor (NR) superfamily. They function as transcriptional repressors by binding to receptor-associated orphan receptor elements in target genes, resulting in chromatin condensation and transcriptional silencing[4]. While primarily recognized for their role in circadian rhythm regulation, REV-ERBα has recently been identified as a key regulator of metabolism and cell survival. Most recently, REV-ERBα has been implicated in the pathogenesis of various metabolic and cardiovascular diseases[5-8].

Mitochondrial homeostasis, encompassing mitochondrial biogenesis, dynamic changes, and the process of mitochondrial autophagy, is associated with various cardiovascular diseases, including PAH[9,10]. Targeting mitochondrial homeostasis has emerged as a promising strategy to

mitigate pulmonary vascular remodeling and retard PAH. Notably, REV-ERBs have been extensively studied for their roles in maintaining mitochondrial homeostasis in tissues such as aortic smooth muscle, skeletal muscle and adipose tissues[11-14]. However, the role of REV-ERBs in PAH progression, particularly their function within pulmonary vascular smooth muscle cells and their relationship with mitochondrial homeostasis, remains poorly explored.

Here we aimed to examine the role of REV-ERBs in the pathogenesis of PAH and to explore how they regulate mitochondrial homeostasis in pulmonary vascular smooth muscle cells.

Results

1. REV-ERBα, but not REV-ERBβ, is downregulated in PAH models

The protein level of REV-ERBα was decreased in lung tissues of SuHx-induced PAH mice (Figure 1A). Immunofluorescence co-staining of α-smooth muscle actin (α-SMA) and REV-ERBα further confirmed the specific decrease of REV-ERBα in primary cultured PASMCs (Figure 1B). Quantitative PCR (qPCR) also showed a significant down-regulation of *Rev-erbα* mRNA in pulmonary arteries of the SuHx mice (Figure 1C). Moreover, to investigate whether this downregulation was a direct response to hypoxia, we subjected isolated PASMCs to either physical hypoxia or treatment with cobalt chloride ($CoCl_2$), a well-established hypoxia mimetic agent[15,16]. REV-ERBα expression was significantly decreased in $CoCl_2$-treated (Figure 1D-F) or hypoxia-exposed (Figure 1G-I) PASMCs as well. In contrast, REV-ERBβ expression remained unchanged in either lung tissues, pulmonary arteries or PASMCs (Figure S1A-I). Additionally, considering the crosstalk effects between hypoxia and the circadian clock, we characterized the expression of other core circadian genes in lung tissue from the SuHx mice and hypoxia-exposed PASMCs. While we did observe modest fluctuations in the protein expression of CRY1 and PER1 and the transcriptional amplitude of *Cry1* and *Per1* in PASMCs, the most consistent, profound, and statistically significant change was the downregulation of REV-ERBα (Figure S2A-I). These findings suggest REV-ERBα may participate in pulmonary vascular remodeling and PAH development.

2. SR9009 attenuates hypoxia-induced PASMC proliferation in a REV-ERBα-dependent

manner

Proliferation of PASMCs is a key event in the pathogenesis of pulmonary vascular remodeling and PAH[1]. To further investigate the role of REV-ERBs in PASMC proliferation, we treated PASMCs with SR9009, a small-molecule agonist targeting REV-ERBs[17]. The data showed that SR9009 significantly suppressed hypoxia-induced PASMC proliferation, as demonstrated by reduced EdU incorporation, fewer Ki67-positive cells, and lower Cell Counting Kit-8 (CCK-8) assay results (Figure 2A-B, Figure S3A). Considering that SR9009 may exhibit off-target pharmacological effects on REV-ERBs[18,19], we knocked down *Rev-erbs* with siRNA in hypoxic PASMCs. Notably, knockdown of *Rev-erbα* not only significantly enhanced hypoxia-induced proliferation, but also abrogated the anti-proliferative effect of SR9009 (Figure 2C-D, Figure S3B). In contrast, knockdown of *Rev-erbβ* neither affected hypoxia-induced proliferation nor blocked SR9009's protective effects (Figure S3C-D). To further confirm the role of REV-ERBα in PASMC proliferation, we transfected a *Rev-erbα* overexpression plasmid into PASMCs and found that overexpression of *Rev-erbα* significantly inhibited hypoxia-induced cell proliferation (Figure 2E-F, Figure S3E). These findings collectively demonstrate that REV-ERBα, but not REV-ERBβ, plays a critical role in inhibiting hypoxia-induced PASMC proliferation, and that SR9009 exerts its effects specifically through activation of REV-ERBα.

3. SR9009 mitigates SuHx-induced PAH both during disease development and after its establishment

We next explored the effect of SR9009 on the development of PAH. Mice were given a daily intraperitoneal injection of SR9009 starting at the initiation of SuHx induction (Figure 3A). The results showed that while SR9009 did not change the basal levels of PAH-related parameters in normoxic mice, it significantly attenuated the increased right ventricular systolic pressure (RVSP) and expanded pulmonary artery (PA) wall thickness in the SuHx-induced mice (Figure 3B-C). Echocardiography confirmed that pulmonary acceleration time/pulmonary ejection time (PAT/PET) ratio, a measure of RV afterload correlated with RVSP, was significantly reduced in SuHx mice, and SR9009 effectively restored this decrease (Figure 3D). Pulmonary angiography

assessed structural remodeling in small pulmonary vessels, revealing that SuHx treatment reduced total branch length, branch number, and junctions, and SR9009 rescued these changes (Figure 3E). Additionally, SuHx-induced RV remodeling assessed by Fulton index and wheat germ agglutinin (WGA) staining were also significantly mitigated by SR9009 (Figure 3F-G). Fractional area change (FAC), a parameter for evaluating right ventricular systolic function, was decreased in SuHx mice, and this decline was reversed by SR9009 treatment (Figure S4A).

We also evaluated the therapeutic effect of SR9009 on the established PAH by initiating the once-daily treatment of SR9009 at the beginning of the third week after SuHx induction (Figure S5A). As expected, SR9009 demonstrated clear therapeutic potential on PAH, reversing the pulmonary vascular remodeling and mitigating RV remodeling in SuHx-induced PAH mice (Figure S5B-F). These results indicated that SR9009 treatment can alleviate the progression of PAH and limit pulmonary vascular remodeling, both during the development and after the establishment of PAH.

4. Deficiency of *Rev-erbα* aggravates, while *Rev-erbα* overexpression alleviates, SuHx-induced PAH

Next, we sought to investigate the effect of genetic disruption of REV-ERBs on SuHx-induced PAH progression. To circumvent the developmental abnormalities and reproductive deficiencies associated with *Rev-erbα* global knockout mice[20], heterozygous *Rev-erbα* knockout (*Rev-erbα*$^{+/-}$) mice were utilized and subjected to SuHx-induced PAH with or without SR9009 treatment (Figure 4A, Figure S6A-D). As shown, compared to the *Rev-erbα*$^{+/+}$ control mice, *Rev-erbα*$^{+/-}$ mice displayed exacerbated SuHx-induced PAH, characterized by increased RVSP and PA wall thickness. Notably, these pathological changes were not mitigated by SR9009 treatment (Figure 4B-C). PAT/PET ratio, pulmonary angiography, Fulton index, and WGA staining further verified that *Rev-erbα* haploinsufficiency significantly augmented the SuHx-induced arterial remodeling and RV dysfunction, and SR9009 failed to confer protection under this genetic background (Figure 4D-G).

To further explore isoform-specific roles, we employed *Rev-erbβ*$^{-/-}$ mice to assess the impact

of *Rev-erbβ* depletion on PAH. In contrast to the *Rev-erbα* deficiency, *Rev-erbβ* knockout did not alter PAH phenotypes following SuHx induction, as PAH-related parameters in *Rev-erbβ*$^{-/-}$ mice after SuHx induction were comparable to those in their wild-type littermates (Figure S6E-G, S7A-F). Collectively, these findings strongly indicate that REV-ERBα, but not REV-ERBβ, plays a pivotal role in the pathogenesis of experimental PAH.

Furthermore, we validated the protective function of REV-ERBα in PAH by establishing a *Rev-erbα* overexpression mouse model through tail vein injection of an adeno-associated virus (AAV) encoding mouse *Rev-erbα*, followed by exposure of these mice to the SuHx-induced PAH (Figure 5A, Figure S8). As expected, *Rev-erbα* overexpression significantly alleviated SuHx-induced PAH, pulmonary vascular and RV remodeling, as evidenced by a reduction in the RVSP (Figure 5B) and PA wall thickness (Figure 5C), alongside an increase in the PAT/PET ratio (Figure 5D), and a lower Fulton index (Figure S9A) and smaller cross-sectional area of RV cardiomyocytes (Figure 5E). These findings further highlight the therapeutic potential of targeting Rev-erbα in PAH.

5. VSMC-specific deletion of *Rev-erbα* aggravates SuHx-induced PAH

Building on the findings that partial loss of *Rev-erbα* exacerbates PAH and that REV-ERB*α* activation inhibits PASMC proliferation under hypoxic conditions, we then aimed to determine whether the primary role of REV-ERBα in PAH and pulmonary vascular remodeling is mediated through vascular smooth muscle cells. By generating the vascular smooth muscle cell-specific *Rev-erbα* knockout mice (VSMC- *Rev-erbα*$^{-/-}$) and subjected them to SuHx-induced PAH (Figure 5F, Figure S10A-D), we found that VSMC-specific deletion of *Rev-erbα* did not affect the baseline pulmonary vascular phenotype (Figure S11); however, similar to the *Rev-erbα*$^{+/-}$ mice, it drastically exacerbated SuHx-induced PAH and pulmonary vascular remodeling (Figure 5G-K, Figure S9B). These findings collectively provide compelling evidence for a previously unrecognized role for REV-ERBα, particularly VSMC-derived REV-ERBα, as a key mediator in mitigating PAH.

6. REV-ERBα improves mitochondrial homeostasis in PAH by mitigating mitophagy in PASMCs

Emerging evidence suggests that mitochondrial homeostasis plays a crucial role in pulmonary vascular remodeling and PAH[9,21]. REV-ERBα has been implicated in regulating mitochondrial function across various metabolic disorders[11,22]. Next, we sought to establish whether activation of REV-ERBα may improve mitochondrial homeostasis in PAH rodent models. By using Transmission Electron Microscope to study the ultra-structure of mitochondria, we observed significant mitochondrial damage and an increased number of autophagic vesicles in SuHx mice compared to normoxic controls. Notably, SR9009 treatment effectively restored mitochondrial integrity and reduced autophagic vesicles (Figure 6A). Furthermore, pulmonary vascular mitochondrial superoxide levels were assessed using mitoSOX, a marker of reactive oxygen species (ROS) generated during oxidative phosphorylation in the electron transport chain[23], and the mitoSOX level was significantly reduced after intervention of SR9009 (Figure 6B). We next examined the expression of key proteins associated with mitochondrial homeostasis and autophagy. Consistent with TEM findings, SR9009 notably reduced the elevated LC3 II/I ratio, an important indicator of autophagosome activation, observed in SuHx lungs, indicating a mitigation of excessive autophagy (Figure 6C). Supporting these findings, immunofluorescence analysis revealed a significant increase in LC3-positive smooth muscle layers within the pulmonary arteries of SuHx mice compared to normoxic controls, which was significantly reversed by SR9009 treatment (Figure 6D), implying SR9009 modulates mitochondrial homeostasis in vascular smooth muscle cells. Consistent with the *in vivo* findings, hypoxic PASMCs showed increased total ROS, decreased mitochondrial membrane potential, elevated mitoSOX, and increased mitophagy, as shown by a higher mt-Keima fluorescence intensity ratio, while SR9009 markedly rescued these changes, restored mitochondrial function and reduced mitophagy (Figure 6E-H). Additionally, SR9009 normalized the LC3 II/I ratio, TOMM20 and P62 protein levels without affecting mitochondrial dynamics or biosynthesis (Figure 6I, Figure S12A-B); notably, the hypoxia-induced conversion of LC3B-I to LC3B-II and the decrease in P62 were reversed by SR9009 in mitochondrial fractions (Figure S12C), further supporting its role in maintaining mitochondrial

homeostasis through mitophagy.

In contrast to the effects of REV-ERBα activation by SR9009, *Rev-erbα*$^{+/-}$ mice demonstrated worsening SuHx-induced autophagy and mitochondrial homeostasis, characterized by elevated mitoSOX levels, increased LC3 II/I ratio, and expanded LC3-positive smooth muscle layer areas compared to the control mice (Figure S13A-C). As expected, SR9009 treatment failed to alter these parameters in *Rev-erbα*$^{+/-}$ mice (Figure S13A-C), further emphasizing the REV-ERBα-dependent mechanism underlying SR9009's effects. Together, these findings suggest that REV-ERBα activation improves mitochondrial homeostasis in PAH by mitigating mitophagy in PASMCs.

7. REV-ERBα regulates mitophagy through transcriptional repression of *Bnip3*

Mitophagy involves two main mechanisms: (A) PINK1-PARKIN mediated ubiquitination pathway, and (B) receptor-mediated processes[24]. To further explore the mechanisms by which REV-ERBα regulates mitophagy, we examined the protein expression of the key mitophagy-related proteins in hypoxia-exposed PASMCs with or without SR9009 treatment. While the non-classical mitophagy receptors BNIP3 and BNIP3L were significantly upregulated in hypoxic PASMCs and notably downregulated by SR9009 treatment, SR9009 did not affect the expression of HIF1A, FUNDC1, PINK1 or PARKIN (Figure 7A, Figure S14A). Importantly, co-immunoprecipitation assays further revealed enhanced interaction between BNIP3/BNIP3L and LC3B under hypoxic conditions, which was attenuated by SR9009 treatment (Figure 7C). Simultaneously, mitochondrial isolation revealed that hypoxia-induced accumulation of BNIP3 in the mitochondrial fraction was also reduced by SR9009 (Figure S12C). Moreover, we found that hypoxia significantly upregulated the anti-apoptotic protein BCL2 without altering the levels of its pro-apoptotic counterpart, BAX, whereas SR9009 had no effect on either protein (Figure S14B). Overall, these findings imply that Rev-erbα regulates BNIP3 and BNIP3L-mediated mitophagy rather than apoptosis.

Intriguingly, SR9009 was observed to significantly mitigate the increase in *Bnip3* mRNA levels, while having no significant effect on *Bnip3l* mRNA levels (Figure 7B), implying that *Bnip3*,

but not *Bnip3l*, might be under direct transcriptional regulation by the transcriptional repressor REV-ERBα. Using the JASPAR database, we identified two potential REV-ERBα binding sites on the *Bnip3* promoter (Figure 7D). Chromatin immunoprecipitation (ChIP) assays performed on cultured PASMCs confirmed that REV-ERBα directly binds to the two regions of the *Bnip3* promoter (Figure 7E). Additionally, dual-luciferase reporter assay showed that overexpression of *Rev-erbα* weakened the luciferase activity in cells transfected with a wild-type *Bnip3* luciferase plasmids (Figure 7F). Strikingly, when *Bnip3* was overexpressed, REV-ERBα lost its inhibitory effect on cell proliferation (Figure 7G-I). These findings strongly suggest that REV-ERBα regulates mitophagy and cell proliferation by transcriptionally repression of *Bnip3* (Figure 7J).

To further establish the role of mitophagy in hypoxia-induced PASMC proliferation and mitochondrial dysfunction, we treated the hypoxia-exposed PASMCs with or without mdivi-1, a widely used mitophagy inhibitor[25-27], and found that mdivi-1 not only significantly attenuated hypoxia-induced proliferation in PASMCs but also blunted the enhanced proliferation observed in *Bnip3*-overexpressing cells (Figure S15-S17). Moreover, we found that overexpression of *Bnip3* in hypoxic PASMCs did not alter BAX expression (Figure S14C). These results collectively indicate that BNIP3 promotes hypoxia-induced PASMC proliferation through a mitophagy-dependent pathway.

Interestingly, an alternatively spliced variant lacking exon 3, termed *Bnip3*Δexon3, has been identified as a pro-survival isoform of *Bnip3* in cardiomyocytes[28,29]. Consequently, the ratio of *Bnip3*Δexon3 to full-length *Bnip3* (*Bnip3*-FL) is considered a critical determinant of whether BNIP3 signaling culminates in cell survival or death[30,31]. Here we confirmed the expression of both *Bnip3*-FL and the shorter *Bnip3*Δexon3 splice variant in PASMCs (Figure S18A-C). Then we found that activation of REV-ERBα by SR9009 not only suppressed the expression of both *Bnip3*Δexon3 and *Bnip3*-FL in hypoxia-exposed PASMCs (Figure S18D-E), but it also significantly decreased the ratio of *Bnip3*Δexon3 to *Bnip3*-FL (Figure S18F).

8. Suppression of *Bnip3* mitigates hypoxic PASMC proliferation, while VSMC-specific *Bnip3* overexpression worsens PAH

As demonstrated above, overexpression of *Bnip3* alone can enhance hypoxia-induced proliferation of PASMCs (Figure 7G-I), indicating its potential role as an independent driver for pulmonary vascular remodeling. To further validate this, we performed *Bnip3* knockdown using siRNA in hypoxic PASMCs. As shown, like the effects of pharmacological activation by SR9009, knockdown of *Bnip3* significantly inhibited hypoxia-induced proliferation of PASMCs and suppressed mitophagy (Figure 8A-C, Figure S19A-E), suggesting that BNIP3 plays a critical role in promoting PASMC proliferation under hypoxic conditions. Finally, we generated a VSMC-specific *Bnip3* overexpression model by tail vein injecting of an AAV carrying *Bnip3* under the control of SM22α promoter, and then exposed them to SuHx-induced PAH (Figure 8D, Figure S20A). As expected, AAV-mediated VSMC-specific *Bnip3* overexpression significantly exacerbated both pulmonary vascular remodeling and RV hypertrophy in the SuHx-PAH model, as evidenced by a higher Fulton index (Figure 8E), a significant increase in RVSP (Figure 8F), pronounced thickening of the PA wall (Figure 8G), a notable decrease in the PAT/PET ratio (Figure 8H), and enlarged cross-sectional area of RV cardiomyocytes (Figure 8I). Taken together, these findings establish vascular smooth muscle-derived BNIP3 as a critical mediator of PAH pathogenesis in murine models.

Discussion

The nuclear receptor REV-ERBs are well-established regulators of circadian rhythms and metabolic homeostasis, yet their role in PAH remains incompletely understood. Here, we demonstrate a selective downregulation of REV-ERBα, but not REV-ERBβ, in pulmonary artery smooth muscle cells (PASMCs) from mice with Su5416/hypoxia (SuHx)-induced PAH, and in primary cultured rat PASMCs subjected to hypoxic conditions (3% O_2 or cobalt chloride-induced chemical hypoxia). Both global and VSMC-specific *Rev-erbα* depletion worsens pulmonary vascular and right heart remodeling in PAH, whereas *Rev-erbβ* depletion had no effect. Moreover, activating REV-ERBα, either through *Rev-erbα* overexpression or pharmacological activation by SR9009, protects against PAH. Mechanistic studies identified *Bnip3* as a direct target trans-

repressed by REV-ERBα, a process that mediates the regulatory effects of REV-ERBα on mitophagy. Conversely, overexpression of *Bnip3* exacerbates hypoxia-induced PASMC proliferation, thereby accelerating pulmonary vascular remodeling and the progression of PAH. In contrast, knockdown of *Bnip3* suppresses hypoxia-induced PASMC proliferation. Overall, these findings highlight that targeting the REV-ERBα-BNIP3 axis could provide a promising strategy for treating and preventing PAH.

Growing evidence demonstrated that REV-ERBα is a critical regulator of metabolic homeostasis, acting at the intersection of circadian biology and energy metabolism[32,33]. As a core component of the circadian clock, REV-ERBα influences the rhythmic expression of genes involved in lipid, glucose, and mitochondrial metabolism[11,20,34,35]. It is also involved in various pathological conditions, such as cancer, metabolic disorders, and many cardiovascular diseases[7,36,37]. Thus, targeting REV-ERBα may retard atherosclerosis, limit abdominal aortic aneurysm formation, and prevent heart failure[22,38,39]. PAH is increasingly recognized as a metabolic homeostasis-related disease, characterized by abnormal vascular remodeling and profound metabolic dysregulation in pulmonary vascular cells[2]. Due to the presence of developmental abnormalities and reproductive disorders in *Rev-erbα* global knockout mice[20], heterozygous *Rev-erbα* knockout mice were utilized in this study. Importantly, our findings indicate that a partial loss of *Rev-erbα* significantly exacerbated PAH, thereby underscoring its critical role in the pathogenesis of PAH. Moreover, through a combination of genetic depletion, overexpression, and pharmacological activation approaches, our study highlights the protective role of REV-ERBα in mitigating PAH, particularly in the SuHx-induced model. Surprisingly, contrasting findings were reported in Pan *et al.*'s most recent study, where REV-ERBα inhibition was shown to mitigate PAH via suppression of mitochondrial fission[40]. This divergence may stem, at least in part, from variations in experimental models: intermittent hypoxia-induced PAH in Pan *et al.*'s study mimics WHO Group 3 hypoxic pulmonary hypertension, whereas the SuHx-induced PAH model used in the current study primarily recapitulates a mixed phenotype of WHO Group 1 (arterial) and Group 3 (hypoxic) pulmonary hypertension[41]. Interestingly, REV-ERBα expression

was upregulated in the intermittent hypoxia model[40], whereas it was downregulated both in the current SuHx model and in the 6% continuous hypoxia model reported by Manella *et al.*[42]. We assume that the intermittent hypoxia model involves cyclical oxygen deprivation, which may uniquely influence molecular signaling pathways compared to sustained hypoxia or SuHx exposure. Nevertheless, these disparities highlight the context-dependent regulation of pulmonary vascular remodeling by REV-ERBα in PAH pathogenesis; therefore, further research is still required to unravel the therapeutic potential of Rev-erbα across diverse experimental models and clinical conditions.

A critical finding of our study is the identification of vascular smooth muscle cell as the primary cell type responsible for REV-ERBα's protective effect in PAH. The proliferation of PASMCs plays a crucial role in pulmonary artery remodeling in PAH, with PASMCs from animal models of PAH and human tissues with PAH exhibiting a metabolic reprogramming pattern similar to cancer cells[43]. In our study, both *Rev-erbα* overexpression and SR9009 treatment inhibited hypoxic PASMC proliferation, while *Rev-erbα* knockdown enhanced cell proliferation. Consistent with the in vitro data, VSMC-specific deletion of *Rev-erbα* exacerbated SuHx-induced PAH compared to wild-type littermates, highlighting the previously unrecognized critical role of VSMC-derived REV-ERBα in the pathogenesis of PAH. However, while endothelial cells, macrophages, and other immune cells also contribute to PAH[44-47], the cell-specific role of REV-ERBα in PAH has yet to be fully explored. We assume that REV-ERBα function may exhibit distinct cardiovascular cell-specific effects. For example, VSMC-derived REV-ERBα predominantly contributes to the pathogenesis of abdominal aortic aneurysm, whereas myeloid REV-ERBα plays a key role in atherosclerosis[22,38]. Additionally, REV-ERBα in platelets has been typically implicated in thrombosis[6]. This divergent, cell-specific biology may underscore the complexity of REV-ERBα's involvement in cardiovascular diseases. Therefore, additional research is essential to delineate the precise cell-specific functions of REV-ERBα, particularly in the context of PAH vascular remodeling.

REV-ERBβ and REV-ERBα have redundant functions in regulating metabolic diseases[20,48]. It

is particularly noteworthy that, forming a striking contrast to REV-ERBα's well-characterized functions, our comprehensive evaluation, utilizing both *Rev-erbβ*-deficient murine models and cellular knockdown systems, definitively reveals its minimal contribution to PAH pathogenesis, specifically in hypoxia-induced vascular remodeling. This parallel investigation of both receptors in PAH reveals their divergent contributions to hypoxia-driven vascular remodeling.

Our results demonstrate the therapeutic potential of SR9009, a REV-ERBs agonist, in mitigating PAH. SR9009 is one of the several small molecule agonists for REV-ERBs, but it stands out due to its longer biological half-life, which facilitates more consistent and extended animal studies[17]. However, concerns regarding its off-target effects have been raised in recent studies, highlighting the complexity of interpreting its therapeutic effects[18,19]. Therefore, it is critical to investigate whether the benefits observed in our study are specifically mediated by REV-ERBα activation, or if they arise from other potential molecular interactions. Excitingly, our findings, particularly in *Rev-erbα* deficient mice and *Rev-erbα* knockdown cells, provide compelling evidence that SR9009 alleviates PAH through a REV-ERBα-dependent mechanism. These results pave the way for the development of more selective and effective REV-ERBα-targeted therapies to combat PAH.

Mitochondrial homeostasis imbalance, characterized by impaired mitochondrial biogenesis, dysregulated mitochondrial dynamics and abnormal mitophagy, plays a central role in the pathogenesis of PAH[49]. REV-ERBα has been identified as a key regulator of mitochondrial homeostasis across multiple tissues and cell types. For instance, REV-ERBα modulates mitochondrial biogenesis and function in skeletal muscle, thereby enhancing muscle performance[11]. Additionally, REV-ERBα influences mitochondrial metabolism in VSMCs by targeting enzymes such as aconitase-2, which is integral to the tricarboxylic acid cycle[22]. In line with these findings, our study demonstrated that REV-ERBα mitigates increased mitochondrial ROS levels in both pulmonary vessels and PASMCs. These results further reinforce the pivotal role of REV-ERBα in preserving mitochondrial homeostasis and its potential as a therapeutic target for PAH and other cardiovascular diseases. Moreover, REV-ERBα has been implicated in

regulating mitochondrial biogenesis and dynamics in various biological contexts[12,13,50]. In our current study, REV-ERBα modulation did not lead to significant changes in the protein markers associated with these processes. This suggests that the protective effects of REV-ERBα on mitochondrial homeostasis in hypoxic PASMCs may not rely on biogenesis or dynamics but instead involve alternative pathways, such as the regulation of mitophagy.

Mitophagy is regulated through both ubiquitination and non-ubiquitination pathways, involving key proteins such as PINK/PARKIN, BNIP3/BNIP3L, and FUNDC1[51]. While the PINK1/PARKIN pathway is a well-characterized mechanism of mitophagy, our model showed no activation of this pathway in PAH. Instead, we observed significantly elevated expression of FUNDC1 and BNIP3/BNIP3L. However, REV-ERBα activation specifically reversed the upregulation of BNIP3/BNIP3L in both animal and cellular PAH models without affecting FUNDC1 levels, suggesting that BNIP3/BNIP3L may serve as the primary mitophagy mediators through which REV-ERBα exerts its protective effects. With the use of mdivi-1, a widely used mitophagy inhibitor, we further demonstrated that BNIP3 promotes hypoxia-induced PASMC proliferation through a mitophagy-dependent pathway. Intriguingly, while mitophagy inhibition usually worsens mitochondrial function, our current data and findings from other studies suggest that, under certain specific stress conditions, suppressing mitophagy may help preserve mitochondrial integrity[52-54]. This observation underscores the complex and context-dependent role of autophagy in maintaining cellular homeostasis. However, we must admit that the mitophagy inhibitor used in this study is not highly specific, and that direct *in vivo* evidence remains lacking. Therefore, further investigations will be required to strengthen and refine these findings in the future. Furthermore, although our current finding mainly points to the major role of BNIP3-mediated mitophagy in PASMC proliferation and PAH, other BNIP3-induced mitochondrial perturbations may also participate in REV-ERBα associated PASMC proliferation and PAH development. Future studies will be necessary to further delineate the relative contributions of BNIP3-induced mitophagy and apoptosis, as well as to elucidate how BNIP3 interacts with other mitochondrial quality control pathways under hypoxic conditions.

Furthermore, we confirmed that REV-ERBα can directly inhibit *Bnip3* transcription by binding to its promoter. Functionally, *Bnip3* knockdown dramatically inhibited hypoxia-induced PASMC proliferation, whereas *Bnip3* overexpression not only negated the anti-proliferative effects of REV-ERBα but also significantly enhanced PASMC proliferation under hypoxic conditions. *In vivo* experiments further revealed that AAV-mediated VSMC-specific *Bnip3* overexpression exacerbated pulmonary vascular and right ventricular remodeling, highlighting BNIP3 as a crucial driver of PAH pathology. To our knowledge, this is the first study to demonstrate the pathological significance of BNIP3 in PAH and to propose it as a potential therapeutic target. Notably, previous research has shown that BMAL1, a core circadian transcription factor and a downstream target negatively regulated by REV-ERBα, can also regulate *Bnip3* to influence mitochondrial homeostasis and contribute to the progression of cardiac hypertrophy[55]. Moreover, *Bnip3* expression is regulated by HIF1A, which in turn exhibits significant functional overlaps with the BMAL1/CLOCK heterodimer, sharing target genes and mutually influencing each other's activity[42,56-58]. While our data suggest a primary role for the REV-ERBα/BNIP3 axis in PAH pathogenesis, future studies could explore whether chronic hypoxia in PAH disrupts the entire circadian network to exacerbate the disease, given that hypoxia is known to cause multiple core circadian rhythm disturbances[42,56,59,60]. In any case, these results suggesting that targeting the circadian clock-mitochondrial health axis, particularly the REV-ERBα–BNIP3 pathway, may represent a promising therapeutic strategy for PAH and other metabolism-related cardiovascular diseases.

Another interesting finding of this study is the demonstration of a hypoxia-induced alternative splicing program for *Bnip3* in PASMCs, resulting in the concurrent expression of both the full-length transcript (*Bnip3*-FL) and a splice variant lacking exon 3 (*Bnip3*Δexon3). This observation is particularly noteworthy when viewed in the context of prior research in cardiomyocytes, where *Bnip3*Δexon3 functions as a pro-survival isoform that antagonizes its pro-death counterpart, establishing the *Bnip3*Δexon3/*Bnip3*-FL ratio as a critical rheostat for cell fate decisions[28-31]. Building upon this, we demonstrated that activation of the nuclear receptor REV-ERBα not only

suppressed the expression of both *Bnip3* isoforms but, more critically, induced a significant reduction in the *Bnip3*Δexon3/*Bnip3*-FL ratio, suggesting that REV-ERBα may shift the cellular balance away from a pro-survival state in hypoxic PASMCs. Although the precise functional consequences of these two variants and the modulation of their ratio within PASMCs have yet to be elucidated, these results identify a potentially crucial mechanism in pulmonary vascular pathobiology that warrants in-depth investigation.

Overall, this study highlights the REV-ERBα-BNIP3 axis as a pivotal regulator of mitochondrial homeostasis and pulmonary vascular remodeling, underscoring its potential as a promising therapeutic target for the prevention and treatment of PAH. Nonetheless, an important limitation of our work is the lack of direct validation in human tissues or clinical cohorts. Although our experimental models provide strong mechanistic support, the clinical relevance of circadian regulators—including REV-ERBα—remains to be fully defined, as human studies often face challenges such as limited sample availability, disease heterogeneity, and the influence of circadian timing on gene expression. Future investigations integrating well-characterized patient samples, ideally with controlled or documented timing of collection, will be essential for determining whether dysregulation of the REV-ERBα-BNIP3 axis occurs in human PAH. Moreover, studies using patient-derived PASMCs and prospective clinical cohorts will help clarify the translational potential of targeting this pathway. Such efforts will be critical to bridge the gap between the current basic mechanistic findings and their application in developing effective circadian-based therapeutic strategies for PAH.

Methods

Animals

Male mice on a C57BL/6N background, aged (8-10 weeks old), were used for all studies. Heterozygous *Rev-erbα* knockout (*Rev-erbα*$^{+/-}$) mice, *Rev-erbβ* global knockout (*Rev-erbβ*$^{-/-}$) mice and their littermate control (*Rev-erbα*$^{+/+}$, *Rev-erbβ*$^{+/+}$) mice were obtained from the Cyagen Company (Suzhou, China). Vascular smooth muscle cell-specific Rev-erbα knockout (VSMC-*Rev-erbα*$^{-/-}$) mice were generated by crossing *Rev-erbα*$^{flox/flox}$ mice with SM22α-Cre^{+} transgenic mice, *Rev-erbα*$^{flox/flox}$ mice that do not express SM22α Cre were used as controls (VSMC-Rev-erbα$^{flox/flox}$, abbreviated as VSMC-Rev-erbα$^{fl/fl}$). Male Sprague-Dawley (SD) rats (8-10 weeks old, weighing 200-250 g) were used for primary cell isolation. All mice were exposed to normal light (lights on at 8 a.m., ZT0 [Zeitgeber Time 0])/dark (lights off at 8 p.m., ZT12 [Zeitgeber Time 12]) cycle with free access to food and water, maintained at an ambient temperature of 22 ± 2 °C and a relative humidity of 50 ± 10%. All animal sacrifices and key physiological measurements were performed between ZT6 and ZT8. All animal experiments were performed conforming to the Institutional Animal Care and Use Committee (IACUC) at East China Normal University (permission number: m+R20211103). All the animal experiments were designed to generate groups using randomization.

PAH model

A hypoxia+Su5416 (SuHx)-induced PAH model in mice were established as follows[61]. In brief, 8-10-week-old male C57BL/6N mice were subcutaneously injected with Su5416 (20 mg/kg, dissolved in a vehicle consisting of 10% DMSO, 40% PEG300, 5% Tween-80, and 45% saline) once a week during the 3-week exposure to a hypoxic chamber. Mice underwent cardiac color Doppler ultrasound examination one day before sacrifice. On the final day of the experiment, animals were fully anesthetized via 2% isoflurane inhalation, and the right ventricular pressure (RVP) was immediately measured using a PT-102N pressure transducer (TECHMAN), carefully inserted into the right ventricle (RV). Hemodynamic values were recorded using a physiological data acquisition system (BL-420N, TECHMAN), and right ventricular systolic pressure (RVSP)

was subsequently calculated. After the measurement of hemodynamic parameters, animals were euthanized via an overdose of isoflurane anesthesia. For the assessment of RV hypertrophy, after euthanasia, the RV was dissected from the left ventricle and interventricular septum and weighed separately. The weight ratio was then calculated as the ratio of weight of the RV to that of the left ventricle plus the inter-ventricular septum. Data acquisition and analysis were performed by an investigator blinded to the experimental groups. Variations in sample sizes among different assessments within the same animal cohort are due to technical failures during specific procedures (e.g., failure in RVSP measurement) or unexpected mortality during the PAH induction period.

Cell culture

Primary male rat PASMCs were isolated as we previously described[61]. In brief, pulmonary arteries were isolated under anatomic microscope and dissected out in dissociation medium from adult Sprague-Dawley (SD) rat (Beijing Vital River Laboratory Animal Technology Co., Ltd.). The tissues were digested by 8.5 mg/mL type I collagenase and 2.0 mg/mL BSA dissolved in $Ca2^{+}$/$Mg2^{+}$-free Hank's Balanced Salt Solution supplemented with 1% Penicillin-Streptomycin (P/S) incubated for 1 h at 37 °C. Then, the cells were cultured in DMEM supplemented with 20% fetal bovine serum, 1% P/S and in a humidified incubator with 95% air and 5% CO_2. Cells between passages 3 and 6 were used for further experiments. PASMCs in hypoxic conditions were incubated for 24 h with a gas mixture containing 3% O_2, 5% CO_2, and 92% N_2, or treated with Cobalt Chloride ($CoCl_2$) (100μM) for 24 h. Human embryonic kidney 293T (HEK293T) cells were obtained from the American Type Culture Collection (ATCC). HEK293T cells were cultured in DMEM supplemented with 10% FBS and 1% P/S and maintained in a humidified incubator with 95% air and 5% CO2 at 37 °C. Both cell types were seeded in standard cell culture dishes or plates (Jet Biofil).

Drug treatment

For the *in vivo* experiment, SR9009 was prepared in 5% DMSO, 10% Cremophor EL, 85% Saline, and administered intraperitoneally at 100 mg/kg once daily between ZT6-ZT8 for a total duration of 21 days of hypoxia or only for the last week of the experiment. The vehicle group

received an equal volume of the identical solvent mixture.

For cell culture experiment, SR9009 (10 μM) was added to the medium for 24 h. Equal concentrations of the solvent DMSO were used as controls. Mitophagy inhibitor mdivi-1 (5 μM) was incubated with cells in the medium for 24 h. Equal concentrations of the solvent DMSO were used as controls.

Echocardiographic measurements

Pulmonary arterial hemodynamics and RV function in the rodent models were assessed by echocardiography. Briefly, the mice were anesthetized with 2% isoflurane and kept warm with a heating plate and then subjected to transthoracic echo using the Vevo 3100 system (VisualSonics) with MX400 (20-46 MHz). The pulmonary artery blood outflow was recorded by Pulsed Wave (PW) Doppler echo in the parasternal short axis view of aortic root and used to measure pulmonary acceleration time (PAT) and pulmonary ejection time (PET). All variables were analyzed from 3 through 5 consecutive peaks or images using Vevo LAB 3.1.1 software (VisualSonics). RV fractional area change was measured in B-mode echocardiograms from the apical 4-chamber view. RV fractional area change (FAC) = (RV end-diastolic chamber area- RV end-systolic chamber area)/RV end-diastolic chamber area. Data acquisition and analysis were performed by an investigator blinded to the experimental groups.

Wheat germ agglutinin

To analyze the cross-sectional area of cardiomyocytes, right heart tissues were stained with wheat germ agglutinin (WGA, Sigma Aldrich, L4895) according to the manufacturer's instructions. Briefly, mice hearts were dehydrated, embedded in paraffin, cut into 5-μm-thick sections. Paraffin sections were heated in a pressure cooker with Tris-EDTA buffer for 3 min. The sections were stained with WGA working solution (Dissolved in water, 1mg/mL) for 30 min at 37 ℃. Stained sections were scanned under an upright fluorescence microscope (Olympus, BX53). ImageJ software (NIH) was used to estimate the cross-sectional area of the cardiomyocytes.

Histology analysis

The right lungs and pulmonary arteries were collected and placed in liquid nitrogen

immediately for preparation of protein and RNA, and the left lungs and part of heart were fixed with 4% paraformaldehyde. Formalin-fixed paraffin-embedded lung tissue was dehydrated with ethanol gradient, embedded in paraffin, and subsequently cut into 5-μm-thick sections. For histological analysis, the sections were stained with hematoxylin and eosin (HE). Images of the HE-stained sections were captured using a digital slide scanning system (SQS-12P, Shengqiang Technology Co.). Or, sections were subjected to immunofluorescence targeting α-smooth muscle actin (α-SMA). To assess medial wall thickness, 15-20 pulmonary arteries categorized by external diameter (<50 μm and >50 μm) were randomly and blindly selected from each lung. The medial area was determined by subtracting the internal luminal area from the total vessel cross-sectional area. The extent of pulmonary vascular remodeling was then evaluated by calculating the ratio of the medial area to the total cross-sectional area [(Total Area − Luminal Area) / Total Area] using ImageJ software (NIH).

Pulmonary angiography

In a separate cohort of mice dedicated to pulmonary angiography, at the termination of the experiments. Briefly, at the termination of the experiments, the animals were anesthetized and then a thoracotomy was carried out to expose their hearts and lungs. The pulmonary artery was subsequently flushed through the right ventricle with PBS containing sodium heparin. Right lung was perfused through the pulmonary artery with 0.1 mL of Microfil, a liquid silicone-based polymer (MV-122, Flow Tech), which was injected slowly and uniformly using a catheter. The lungs were immersed in PBS to cleanse the tissue surface of stains. Subsequently, they were dehydrated and ultimately placed in methyl salicylate for photographic documentation. Total length of arterial branch, number of arterial branch and number of junctions were calculated using ImageJ software (NIH).

Cell proliferation analysis

PASMCs proliferation was quantified using the Cell Counting Kit (CCK-8, MCE), Ki67 immunofluorescence staining, and the EdU Cell Proliferation Image Kit (Abbkine). For the CCK-8 assay, the culture medium of the PASMCs was removed and replaced with 90 μL DMEM and

10μL CCK8, followed by 1 h incubation. The absorbance values were detected at 450 nm wavelength by a microplate reader (Synergy H1, BioTek Instruments). For the EdU assay, living PASMCs were first incubated with 10 μM EdU for 2 h in the cell culture incubator. Following the incorporation, PASMCs were fixed with 4% paraformaldehyde for 20 min, and then incubated with 0.5% Triton X-100 for 20 min, followed by incubation with the click reaction cocktail (provided in the kit) for 30 min in the dark to detect incorporated EdU. Nuclei were then counterstained with DAPI. Images were collected using an upright fluorescence microscope (Olympus, BX53), and the rate of EdU incorporation in the treatment group was normalized with those of the control group. For the Ki67 Immunofluorescence, Cells were fixed with paraformaldehyde, treated with 0.1% Triton X-100 for 30 min, blocked with 5% goat serum and incubated with Ki67 antibody overnight, followed by incubation with anti-rabbit fluorescently conjugated antibody, photographed using confocal and analyzed for fluorescence data using ImageJ software (NIH).

Immunofluorescence

For tissue immunofluorescence, lung tissues were heated in a pressure cooker with Tris-EDTA buffer for 3 min, and then incubated with the blocking buffer 5% goat serum dissolved in PBS. Tissue sections were then incubated with primary antibody over night at 4°C and followed by the incubation of fluorescently conjugated secondary antibody for 1 h at room temperature. Finally, nuclei were counterstained with DAPI. For the quantitative analysis of fluorescence intensity, at least 20 pulmonary vessels per sample were selected, and the images were captured using a confocal microscope (DF505, Andor Technology) for subsequent analysis. For cell immunofluorescence analysis, PASMCs were fixed with 4% paraformaldehyde followed by permeabilized using 0.3% Triton X-100 in PBS and incubated with the 5% goat serum dissolved in PBS. Cells were then incubated with primary antibody overnight at 4°C and followed by incubation with fluorescently conjugated secondary antibody for 1 h at room temperature. Finally, nuclei were counterstained with DAPI. Antibodies used for immunofluorescence are in Table S2.

Assessment of ROS production

For total ROS, cells were distributed into 96-well black plates and incubated with oxygen radical sensitive probe 5 μM DCFH-DA (S0033S, Beyotime) for 30 min in a 37 °C, 5% CO_2 incubator in the dark, and subsequently measure ROS probe fluorescence intensity with a microplate reader (Synergy H1, BioTek Instruments). For the mitoSOX assay of pulmonary vasculature, fresh lung tissues were embedded in Optimal Cutting Temperature compound, and snap-frozen. Unfixed cryosections were then prepared and topically stained with a 5 μM MitoSOX Red superoxide indicator (Yeason, 40778ES50) in a light-protected, humidified chamber. For each group of mice, at least 20 pulmonary vessels were selected from each mouse's lungs for statistical analysis, with fluorescence images captured using a DF505 fluorescence microscope (Andor Technology) and intensity analyzed via ImageJ software (NIH). Mitochondrial superoxide in PASMCs was detected by staining with 1 μM MitoSOX Red (Invitrogen, M36008) in phenol red-free media for 30 min at 37 °C, followed by two PBS washes. Cells were imaged on an upright fluorescence microscope (Olympus, BX53). For quantification, ten fields of view per sample were acquired with fixed acquisition settings. Fluorescence intensity was quantified for ≥100 cells per condition using ImageJ (NIH). The mean fluorescence intensity was measured within ROIs manually drawn around whole cells.

Measurement of mitochondrial membrane potential (MMP)

The MMP of PASMCs was monitored using JC-1 (J8030, Solarbio). Briefly, PASMCs were incubated in the dark with JC-1 for 30 min at 37 °C and washed with PBS for three times. When the mitochondrial membrane potential is elevated, JC-1 aggregates within the mitochondrial matrix, exhibiting a maximum excitation wavelength of 585 nm and resulting in enhanced red fluorescence. Conversely, when the mitochondrial membrane potential is diminished, JC-1 remains in its monomeric form with a maximum excitation wavelength of 514 nm leading to an increase in green fluorescence. The alteration in mitochondrial membrane potential is assessed by the shift in fluorescence color. The fluorescence images were captured using an upright fluorescence microscope (Olympus, BX53) and the mitochondrial membrane potential was quantified by calculating the ratio of red (aggregates) to green (monomers) fluorescence intensity

using Image J software (NIH).

Chromatin immunoprecipitation (ChIP)

ChIP was performed using anti-REV-ERBα and anti-rabbit IgG. PASMCs were fixed with 1% formaldehyde, and cross-linked protein-DNA complexes were prepared using a ChIP kit. Complexes were incubated with a primary antibody against REV-ERBα or rabbit IgG for 18h at 4°C. Magnetic beads were added with gentle agitation for 2h. DNA was eluted from the beads. Primers flanking the REV-ERBα binding sites on the rat *Bnip3* gene promoter were used in PCR assays, and PCR products were visualized using agarose gel electrophoresis with a chemiluminescence imaging system (Bio-Rad, ChemiDoc XRS+). Primer sequences used for ChIP-PCR are in Table S3.

Co-Immunoprecipitation (Co-IP)

For immunoprecipitation in the endogenous system, PASMCs were seeded 24 h prior to stimulations. After stimulation, PASMCs were lysed in NP-40 lysis buffer. Protein concentrations were determined, and 500 μg of total protein lysate was used for each IP. An aliquot of 10% from each whole-cell lysate was saved as the Input control. Cell lysates were pre-cleared using 20 μl of protein A/G plus-agarose beads (sc-2003, Santa Cruz Biotechnologies) for 2h at 4°C. Primary anti-LC3B antibody was added at a concentration of 1:100 and incubated overnight at 4°C (Normal rabbit IgG was used as a negative control for the immunoprecipitation). The immune complexes were then precipitated by adding 30 μL of Protein A/G plus-agarose beads and incubating for an additional 2 h at 4°C. The beads were subsequently washed three times with lysis buffer, and the immunoprecipitated proteins were eluted by boiling in SDS sample buffer prior to immunoblotting analysis. Antibodies used for immunoprecipitation are in Table S2.

Mitochondrial isolation

Mitochondrial and cytosolic fractions were prepared using a Cell Mitochondria Isolation Kit (C3601, Beyotime Biotechnology). Briefly, cell pellets were lysed via Dounce homogenization. The homogenate was centrifuged at 600 × g for 10 minutes at 4 °C to remove nuclei and cell debris. The resulting supernatant was then centrifuged at 11,000 × g for 10 minutes at 4 °C to pellet

mitochondria. The final supernatant was collected as the cytosolic fraction. Subsequently, both components underwent Western blot analysis, with GAPDH serving as the cytoplasmic protein reference and COX IV as the mitochondrial protein reference. Antibodies used for western blot are listed in Table S2.

Western blot, qPCR

For western blot analysis, protein samples were subjected to SDS-PAGE and transferred to polyvinylidene fluoride (PVDF) membranes. The membranes were incubated overnight with indicated primary antibodies, followed by the appropriate HRP-conjugated secondary antibodies. Finally, immunoblots were visualized with a gel image analysis system (Tanon 5200, Tanon Science & Technology), and the densitometric quantification of protein bands was performed using ImageJ software (NIH). Antibodies used for western blot are in Table S2.

For qPCR analysis, total RNA was extracted by using TRIzol reagent (Invitrogen). The cDNA was obtained using the TIANGEN Reverse Transcription Kit (KR107, TIANGEN) and subsequently the relative mRNA expression levels were quantified using SYBR Green (AQ631, TransGen Biotech) on a Real-Time PCR System (QuantStudio 5, Thermo Scientific), with *18S* as an internal control. The relative mRNA expression levels were calculated using the 2^(-ΔΔCt) method. Primer sequences used for qPCR are in Table S3.

Transmission electron microscopy (TEM)

Lung tissues were harvested and dissected, rinsed in PBS and then fixed in 2.5% glutaraldehyde in PBS. After being washed with PBS three times, the samples were fixed in PBS-buffered 1% OsO4 for 1 h, washed in ddH_2O, stained in uranyl acetate for 30 min, dehydrated in a gradient of ethanol and acetone, permeated by embedding medium containing acetone (1:1), and finally embedded in epoxy resin. The ultrathin electron-stained sections were observed under an electron microscope (Tecnai T10, Philips-FEI) with voltage setting at 100 kV. Micrographs of randomly selected mitochondria were obtained at a final magnification of ×20000.

Plasmids, RNA interference

Recombinant plasmids encoding rat *Bnip3* and rat *Rev-erbα* were purchased from MiaoLing

Plasmid for achieving overexpression of *Bnip3* and *Rev-erbα* in PASMCs. For individual transient transfection, the plasmid was transfected into PASMCs at a final concentration of 0.5 μg/ml with the assistance of Lipofectamine 3000 (Invitrogen) for 48 h. For co-transfection, the plasmids were co-transfected into the cells at half of the aforementioned concentration for 48 h.

Rev-erbα/β siRNA, *Bnip3* siRNA, and negative control siRNA were sourced from Genepharma. In accordance with the experimental requirements, these siRNAs were individually transfected into PASMCs at a final concentration of 25 nM with the aid of Lipofectamine 3000 (Invitrogen). Following transfection, the cells were incubated for 48 h to facilitate effective gene silencing. All siRNA sequences are shown in Table S3.

Adeno-Associated Virus, Adenovirus

For *Rev-erbα* overexpression, adeno-associated virus 9 (AAV9) carrying a CMV-promoter-driven FLAG- Rev-erbα (AAV-OE-*Rev-erbα*) or negative control was administered intravenously in a single dose of 5×10^{11} v.g./mouse. Mice were subjected to SuHx-induced PAH one week after AAV9 injection. For VSMC-specific *Bnip3* overexpression, AAV9 carrying a SM22α-promoter-driven FLAG-*Bnip3* (AAV-OE-*Bnip3*) or negative control was administered intravenously in a single dose of 1×10^{12} v.g./mouse. Mice were subjected to normoxia or SuHx treatment one week after AAV9 injection. All viruses were constructed and purified by Obio Technology (Obio Technology Corp).

A mitochondria-targeted Keima adenovirus (Adv-COX8-mt-Keima) (Obio Technology Corp) was employed to evaluate mitophagy in PASMCs, which were infected with the recombinant virus at a multiplicity of infection (MOI) of 100 for 48 h. Mitochondria-targeted Keima (Mt-Keima) is a pH-sensitive fluorescent protein that shifts its excitation peak to 561 nm in lysosomal acidic conditions, compared to 445 nm in other environments. The quantification of mitophagy can be achieved through the detection of mt-Keima fluorescence shift[62].

Dual-Luciferase Reporter assay

The dual-luciferase reporter assay was conducted according to the technical manual of Promega Dual-Luciferase Reporter Assay System (E1910, Promega). Firefly luciferase assays

were carried out using the luciferase reporter vector pGL4.11-Basic, engineered to contain the wild-type promoter region of *Bnip3* (rat), resulting in vectors termed *Bnip3*-promoter-luc. The firefly reporter plasmid, Renilla luciferase internal control plasmid, and the *Rev-erbα* overexpression plasmid (or empty vector control) were co-transfected into HEK293T cells (ATCC) by Lipofectamine 3000. After 24 h, cells were homogenized by the passive lysate buffer provided by the manufacturer. Luciferase Assay Reagent II and Stop and Glo Reagent were added to the lysates sequentially. Luminous intensity was detected by the microplate reader using the luminescence model.

Reagents

The reagents utilized in the current study have been outlined in Table S1.

Statistical analysis

Statistical analyses were performed using Prism 8 software (GraphPad). All results are reported as the mean ± SEM. No statistical methods were used to predetermine sample sizes. Sample sizes were chosen based on standard protocols in the field and our previous similar studies. For all animal experiments, *n* represents the number of individual animals. For cell culture experiments, *n* represents the number of independent biological replicates. For groups with $n > 3$, the normality of data distribution was evaluated using the Shapiro-Wilk test. For groups with $n = 3$, a normal distribution was assumed based on prior literature and historical data. Statistical differences between two groups were analyzed using two-tailed Student's *t*-tests, whereas differences among multiple groups were analyzed using one-way or two-way ANOVA followed by Tukey's post hoc test. Exact *P* values are annotated directly within the figures, and the specific statistical methods applied to each experiment are detailed in the corresponding figure legends.

Data availability

All data supporting the findings of this study are available within the paper and its Supplementary Information. The source data underlying all main and supplementary figures are provided as a publicly available Source Data file.

References

1. Oldham, W.M.*, et al.* NHLBI-CMREF Workshop Report on Pulmonary Vascular Disease Classification: JACC State-of-the-Art Review. *Journal of the American College of Cardiology* **77**, 2040-2052 (2021).
2. Humbert, M.*, et al.* 2022 ESC/ERS Guidelines for the diagnosis and treatment of pulmonary hypertension. *The European respiratory journal* **61**(2023).
3. Ghofrani, H.A., Gomberg-Maitland, M., Zhao, L. & Grimminger, F. Mechanisms and treatment of pulmonary arterial hypertension. *Nature reviews. Cardiology* **22**, 105-120 (2025).
4. Kim, Y.H.*, et al.* Rev-erbα dynamically modulates chromatin looping to control circadian gene transcription. *Science (New York, N.Y.)* **359**, 1274-1277 (2018).
5. Pourcet, B.*, et al.* Nuclear Receptor Subfamily 1 Group D Member 1 Regulates Circadian Activity of NLRP3 Inflammasome to Reduce the Severity of Fulminant Hepatitis in Mice. *Gastroenterology* **154**, 1449-1464.e1420 (2018).
6. Shi, J.*, et al.* Circadian nuclear receptor Rev-erbα is expressed by platelets and potentiates platelet activation and thrombus formation. *European heart journal* **43**, 2317-2334 (2022).
7. Zhao, Y.*, et al.* Disruption of Circadian Rhythms by Shift Work Exacerbates Reperfusion Injury in Myocardial Infarction. *Journal of the American College of Cardiology* **79**, 2097-2115 (2022).
8. Boulinguiez, A.*, et al.* NR1D1 controls skeletal muscle calcium homeostasis through myoregulin repression. *JCI insight* **7**(2022).
9. Culley, M.K. & Chan, S.Y. Mitochondrial metabolism in pulmonary hypertension: beyond mountains there are mountains. *The Journal of clinical investigation* **128**, 3704-3715 (2018).
10. Li, Q.*, et al.* Knockout of dihydrofolate reductase in mice induces hypertension and abdominal aortic aneurysm via mitochondrial dysfunction. *Redox biology* **24**, 101185 (2019).
11. Woldt, E.*, et al.* Rev-erb-α modulates skeletal muscle oxidative capacity by regulating mitochondrial biogenesis and autophagy. *Nature medicine* **19**, 1039-1046 (2013).
12. Sengupta, S.*, et al.* The circadian gene Rev-erbα improves cellular bioenergetics and provides preconditioning for protection against oxidative stress. *Free radical biology & medicine* **93**, 177-189 (2016).
13. Sun, L.*, et al.* Circadian Clock Genes REV-ERBs Inhibits Granulosa Cells Apoptosis by Regulating Mitochondrial Biogenesis and Autophagy in Polycystic Ovary Syndrome. *Frontiers in cell and developmental biology* **9**, 658112 (2021).
14. Yu, B., Pan, J.B. & Yu, F.Y. The combination of nuclear receptor NR1D1 and ULK1 promotes mitophagy in adipocytes to ameliorate obesity. *Adipocyte* **11**, 202-212 (2022).
15. Marsboom, G.*, et al.* Dynamin-related protein 1-mediated mitochondrial mitotic fission permits hyperproliferation of vascular smooth muscle cells and offers a novel therapeutic target in pulmonary hypertension. *Circulation research* **110**, 1484-1497 (2012).
16. Ryan, J.J.*, et al.* PGC1α-mediated mitofusin-2 deficiency in female rats and humans with pulmonary arterial hypertension. *American journal of respiratory and critical care medicine* **187**, 865-878 (2013).
17. Solt, L.A.*, et al.* Regulation of circadian behaviour and metabolism by synthetic REV-ERB agonists. *Nature* **485**, 62-68 (2012).

18. Dierickx, P., *et al.* SR9009 has REV-ERB-independent effects on cell proliferation and metabolism. *Proceedings of the National Academy of Sciences of the United States of America* **116**, 12147-12152 (2019).
19. Xu, H., *et al.* SR9009 inhibits lethal prostate cancer subtype 1 by regulating the LXRα/FOXM1 pathway independently of REV-ERBs. *Cell death & disease* **13**, 949 (2022).
20. Cho, H., *et al.* Regulation of circadian behaviour and metabolism by REV-ERB-α and REV-ERB-β. *Nature* **485**, 123-127 (2012).
21. Diebold, I., *et al.* BMPR2 preserves mitochondrial function and DNA during reoxygenation to promote endothelial cell survival and reverse pulmonary hypertension. *Cell metabolism* **21**, 596-608 (2015).
22. Sun, L.Y., *et al.* Nuclear Receptor NR1D1 Regulates Abdominal Aortic Aneurysm Development by Targeting the Mitochondrial Tricarboxylic Acid Cycle Enzyme Aconitase-2. *Circulation* **146**, 1591-1609 (2022).
23. Imanishi, M., *et al.* Smooth muscle cell-specific Hif-1α deficiency suppresses angiotensin II-induced vascular remodelling in mice. *Cardiovascular research* **102**, 460-468 (2014).
24. Levine, B. & Kroemer, G. Biological Functions of Autophagy Genes: A Disease Perspective. *Cell* **176**, 11-42 (2019).
25. Jiang, X.L., *et al.* PHLDA1 contributes to hypoxic ischemic brain injury in neonatal rats via inhibiting FUNDC1-mediated mitophagy. *Acta pharmacologica Sinica* **45**, 1809-1820 (2024).
26. Li, X.T., *et al.* The UCP2/PINK1/LC3b-mediated mitophagy is involved in the protection of NRG1 against myocardial ischemia/reperfusion injury. *Redox biology* **80**, 103511 (2025).
27. Li, J., *et al.* Restricting intracellular Salmonella proliferation by coordinating p-TBK1 mediated mitophagy and xenophagy. *Autophagy*, 1-23 (2025).
28. Gang, H., *et al.* A novel hypoxia-inducible spliced variant of mitochondrial death gene Bnip3 promotes survival of ventricular myocytes. *Circulation research* **108**, 1084-1092 (2011).
29. Pandey, A., *et al.* Identification of SRSF9 through pooled shRNA screening links BNIP3 splicing to autophagy and metabolic reprogramming in breast cancer. *The Journal of biological chemistry* **301**, 110482 (2025).
30. Gang, H., *et al.* PDK2-mediated alternative splicing switches Bnip3 from cell death to cell survival. *The Journal of cell biology* **210**, 1101-1115 (2015).
31. Field, J.T., *et al.* Misoprostol regulates Bnip3 repression and alternative splicing to control cellular calcium homeostasis during hypoxic stress. *Cell death discovery* **4**, 37 (2018).
32. Zhang, Y., *et al.* GENE REGULATION. Discrete functions of nuclear receptor Rev-erbα couple metabolism to the clock. *Science (New York, N.Y.)* **348**, 1488-1492 (2015).
33. Wang, S., Li, F., Lin, Y. & Wu, B. Targeting REV-ERBα for therapeutic purposes: promises and challenges. *Theranostics* **10**, 4168-4182 (2020).
34. Hunter, A.L., *et al.* Nuclear receptor REVERBα is a state-dependent regulator of liver energy metabolism. *Proceedings of the National Academy of Sciences of the United States of America* **117**, 25869-25879 (2020).
35. Zhang, Q., *et al.* Recent Advances in Hepatic Metabolic Regulation by the Nuclear Factor Rev-erbα. *Current drug metabolism* **25**, 2-12 (2024).

36. Sulli, G., *et al.* Pharmacological activation of REV-ERBs is lethal in cancer and oncogene-induced senescence. *Nature* **553**, 351-355 (2018).
37. Song, S., *et al.* Myocardial Rev-erb-Mediated Diurnal Metabolic Rhythm and Obesity Paradox. *Circulation* **145**, 448-464 (2022).
38. Ma, H., *et al.* Increased atherosclerotic lesions in LDL receptor deficient mice with hematopoietic nuclear receptor Rev-erbα knock- down. *Journal of the American Heart Association* **2**, e000235 (2013).
39. Reitz, C.J., *et al.* SR9009 administered for one day after myocardial ischemia-reperfusion prevents heart failure in mice by targeting the cardiac inflammasome. *Communications biology* **2**, 353 (2019).
40. Pan, Z., *et al.* Nr1d1 inhibition mitigates intermittent hypoxia-induced pulmonary hypertension via Dusp1-mediated Erk1/2 deactivation and mitochondrial fission attenuation. *Cell death discovery* **10**, 459 (2024).
41. Boucherat, O., Agrawal, V., Lawrie, A. & Bonnet, S. The Latest in Animal Models of Pulmonary Hypertension and Right Ventricular Failure. *Circulation research* **130**, 1466-1486 (2022).
42. Manella, G., *et al.* Hypoxia induces a time- and tissue-specific response that elicits intertissue circadian clock misalignment. *Proceedings of the National Academy of Sciences of the United States of America* **117**, 779-786 (2020).
43. Paulin, R. & Michelakis, E.D. The metabolic theory of pulmonary arterial hypertension. *Circulation research* **115**, 148-164 (2014).
44. Evans, C.E., Cober, N.D., Dai, Z., Stewart, D.J. & Zhao, Y.Y. Endothelial cells in the pathogenesis of pulmonary arterial hypertension. *The European respiratory journal* **58**(2021).
45. Wang, R.R., *et al.* Immunity and inflammation in pulmonary arterial hypertension: From pathophysiology mechanisms to treatment perspective. *Pharmacological research* **180**, 106238 (2022).
46. Al-Qazazi, R., *et al.* Macrophage-NLRP3 Activation Promotes Right Ventricle Failure in Pulmonary Arterial Hypertension. *American journal of respiratory and critical care medicine* **206**, 608-624 (2022).
47. Zhang, M.Q., *et al.* Role of macrophages in pulmonary arterial hypertension. *Frontiers in immunology* **14**, 1152881 (2023).
48. Liu, A.C., *et al.* Redundant function of REV-ERBalpha and beta and non-essential role for Bmal1 cycling in transcriptional regulation of intracellular circadian rhythms. *PLoS genetics* **4**, e1000023 (2008).
49. Ryanto, G.R.T., Suraya, R. & Nagano, T. Mitochondrial Dysfunction in Pulmonary Hypertension. *Antioxidants (Basel, Switzerland)* **12**(2023).
50. Chen, L., *et al.* m(6)A methylation-induced NR1D1 ablation disrupts the HSC circadian clock and promotes hepatic fibrosis. *Pharmacological research* **189**, 106704 (2023).
51. Picca, A., Faitg, J., Auwerx, J., Ferrucci, L. & D'Amico, D. Mitophagy in human health, ageing and disease. *Nature metabolism* **5**, 2047-2061 (2023).
52. Qasim, W., *et al.* PTEN-induced kinase 1-induced dynamin-related protein 1 Ser637 phosphorylation reduces mitochondrial fission and protects against intestinal ischemia reperfusion injury. *World journal of gastroenterology* **26**, 1758-1774 (2020).
53. Lin, Y., *et al.* Targeting DRP1 with Mdivi-1 to correct mitochondrial abnormalities in ADOA+ syndrome. *JCI insight* **9**(2024).

54. Zhang, C., *et al.* Gestational Exposure to Black Phosphorus Nanoparticles Induces Placental Trophoblast Dysfunction by Triggering Reactive Oxygen Species-Regulated Mitophagy. *ACS nano* **19**, 16517-16533 (2025).
55. Li, E., *et al.* BMAL1 regulates mitochondrial fission and mitophagy through mitochondrial protein BNIP3 and is critical in the development of dilated cardiomyopathy. *Protein & cell* **11**, 661-679 (2020).
56. Wu, Y., *et al.* Reciprocal Regulation between the Circadian Clock and Hypoxia Signaling at the Genome Level in Mammals. *Cell metabolism* **25**, 73-85 (2017).
57. Peek, C.B. Metabolic Implications of Circadian-HIF Crosstalk. *Trends in endocrinology and metabolism: TEM* **31**, 459-468 (2020).
58. Dandavate, V., *et al.* Hepatic BMAL1 and HIF1α regulate a time-dependent hypoxic response and prevent hepatopulmonary-like syndrome. *Cell metabolism* **36**, 2038-2053.e2035 (2024).
59. Adamovich, Y., Ladeuix, B., Golik, M., Koeners, M.P. & Asher, G. Rhythmic Oxygen Levels Reset Circadian Clocks through HIF1α. *Cell metabolism* **25**, 93-101 (2017).
60. Wu, G., *et al.* Short-term exposure to intermittent hypoxia leads to changes in gene expression seen in chronic pulmonary disease. *eLife* **10**(2021).
61. Liu, M., *et al.* Maresin-1 protects against pulmonary arterial hypertension by improving mitochondrial homeostasis through ALXR/HSP90α axis. *Journal of molecular and cellular cardiology* **181**, 15-30 (2023).
62. Liu, Y.T., *et al.* Mt-Keima detects PINK1-PRKN mitophagy in vivo with greater sensitivity than mito-QC. *Autophagy* **17**, 3753-3762 (2021).

Acknowledgments

This work was supported by Noncommunicable Chronic Diseases-National Science and Technology Major Project (grant number: 2024ZD0528200 to L.C.) and National Natural Science Foundation of China (grant number: 32571348, 32071157 to L.C.).

Author contributions

Conceptualization: L.Q., G.Y., L.C.

Methodology: L.Q., T.L., J.Z., M.L., H.W., W.L., C.M., S.L., B.R., Q.W., F.F., H.X., F.Z., Y.G., X.Z.

Investigation: L.Q., T.L., J.Z., M.L.

Visualization: L.Q., T.L., J.Z., M.L., W.L.

Supervision: G.Y., L.C.

Writing—original draft: L.Q.

Writing—review & editing: G.Y., L.C.

Competing Interests Statement:

The authors declare no competing interests.

Figure Legends

Figure 1. REV-ERBα is downregulated in SuHx mice and hypoxic PASMCs. (A) Western blot analysis and quantification of REV-ERBα protein expression in lung tissues from normoxic and SuHx mice (*n*=6 mice for normoxia, *n*=7 mice for SuHx). (B) Immunofluorescence staining of REV-ERBα expression in mouse lung tissues, with co-staining for α-SMA; white arrows indicate REV-ERBα localization in the vascular smooth muscle layer. Scale bars: 100 μm (top), 40 μm (middle), and 80 μm (bottom). (C) qPCR quantification of *Rev-erbα* mRNA expression in the isolated pulmonary arteries (*n*=5 independent biological replicates). (D) Western blot analysis of REV-ERBα protein expression in primary cultured PASMCs stimulated with ddH_2O or $CoCl_2$ for 24 h (*n*=6 independent biological replicates). (E) Representative images and quantification of immunofluorescence staining of REV-ERBα in primary cultured PASMCs stimulated with ddH_2O or $CoCl_2$ for 24 h, with nuclear counterstaining by DAPI (*n*=6 independent biological replicates). Scale bars: 30 μm (top) and 60 μm (bottom). (F) qPCR quantification of *Rev-erbα* mRNA expression in primary cultured PASMCs stimulated with ddH_2O or $CoCl_2$ for 24 h (*n*=6 independent biological replicates). (G) Western blot analysis of REV-ERBα protein expression in primary cultured PASMCs exposed to 21% O_2 (normoxia) or 3% O_2 (hypoxia) for 24 h (*n*=6 independent biological replicates). (H) Representative images and quantification of immunofluorescence staining of REV-ERBα expression in primary cultured PASMCs exposed to 21% O_2 (normoxia) or 3% O_2 (hypoxia) for 24 h, with nuclear counterstaining by DAPI (*n*=6 independent biological replicates). Scale bars: 30 μm (top) and 60 μm (bottom). (I) qPCR quantification of *Rev-erbα* mRNA expression in primary cultured PASMCs exposed to 21% O_2 (normoxia) or 3% O_2 (hypoxia) for 24 h (*n*=6 independent biological replicates). All data are presented as means ± SEM. Statistical significance was determined by two-tailed unpaired Student's *t*-test. Source data are provided as a Source Data file.

Figure 2. SR9009 attenuates hypoxia-induced PASMC proliferation in a REV-ERBα-dependent manner. (A-B) PASMCs exposed to 21% O_2 (normoxia) or 3% O_2 (hypoxia) were treated with or without SR9009. (A) Representative images and quantification of EdU incorporation of proliferative PASMCs (*n*=6 independent biological replicates). Scale bars: 100 μm (top) and 200 μm (bottom). (B) Representative images and quantification Ki67 immunofluorescence staining of proliferative PASMCs. Nuclei were counterstained with DAPI (*n*=3 independent biological replicates). Scale bars: 30 μm (top) and 60 μm (bottom). (C-D) Hypoxic PASMCs were transfected with *Rev-erbα* siRNA or the negative control (NC) siRNA for 48 h and then were treated with or without SR9009. (C) Representative images and quantification of EdU incorporation of proliferative PASMCs (*n*=3 independent biological replicates). Scale bars: 150 μm (top) and 300 μm (bottom). (D) Representative images and quantification of Ki67 immunofluorescence staining of proliferative PASMCs. Nuclei were counterstained with DAPI (*n*=3 independent biological replicates). Scale bars: 200 μm (top) and 400 μm (bottom). (E-F) PASMCs exposed to normoxic or hypoxic conditions were transfected with or without the *Rev-erbα* overexpression plasmid for 48 h. (E) Representative images and quantification of EdU incorporation of proliferative PASMCs (*n*=3 independent biological replicates). Scale bars: 150 μm (top) and 300 μm (bottom). (F) Representative images and quantification of Ki67 immunofluorescence staining in PASMCs. Nuclei were counterstained with DAPI (*n*=3 independent biological replicates). Scale bars: 200 μm (top) and 400 μm (bottom). All data are presented as means ± SEM. Statistical significance was determined by two-way ANOVA followed by Tukey's post-hoc test. Source data are provided as a Source Data file.

Figure 3. SR9009 attenuates SuHx-induced PAH in mice. (A) Schematic protocol: WT mice were subjected to normoxia or SuHx and intraperitoneally injected with vehicle or SR9009 for 3 weeks. (B) Representative RVP images and analysis of RVSP (*n*=5 mice for normoxia+ Vehicle, *n*=5 mice for normoxia+ SR9009, *n*=10 mice for SuHx+ Vehicle, and *n*=8 mice for SuHx+ SR9009). The x-axis scale bar indicates 400 ms. (C) Representative images of HE staining and immunofluorescence staining of α-SMA, and

the quantification of ratios of vascular medial thickness to total vessel diameter (*n*=6 mice for normoxia+ Vehicle, *n*=6 mice for normoxia+ SR9009, *n*=11 mice for SuHx+ Vehicle, and *n*=9 mice for SuHx+ SR9009). Scale bar: 50 μm. (D) Echocardiographic analysis of pulmonary artery hemodynamics: pulmonary artery acceleration time (PAT) and ejection time (PET) (*n*=6 mice for normoxia+ Vehicle, *n*=6 mice for normoxia+ SR9009, *n*=10 mice for SuHx+ Vehicle, and *n*=9 mice for SuHx+ SR9009). (E) Representative images of pulmonary angiography and quantification of the branch count, junction count, and total length (*n*=10 mice for normoxia, *n*=9 mice for SuHx, and *n*=6 mice for SuHx+ SR9009). Scale bar: 3 mm. (F) Fulton index [right ventricle weight/ (left ventricle + septum weight), RV/(LV+S)] as a marker of right ventricular (RV) hypertrophy (*n*=5 mice for normoxia+ Vehicle, *n*=5 mice for normoxia+ SR9009, *n*=8 mice for SuHx+ Vehicle, and *n*=7 mice for SuHx+ SR9009). (G) Representative images of wheat germ agglutinin (WGA) staining and the quantitative analysis of cardiomyocyte cross-sectional area (*n*=5 mice for normoxia+ Vehicle, *n*=5 mice for normoxia+ SR9009, *n*=8 mice for SuHx+ Vehicle, and *n*=7 mice for SuHx+ SR9009). Scale bars: 200 μm (top) and 50 μm (bottom). All data are presented as means ± SEM. Statistical significance was determined by one-way ANOVA followed by Tukey's post-hoc test for E, and two-way ANOVA followed by Tukey's post-hoc test for all other panels. Source data are provided as a Source Data file.

Figure 4. Deficiency of *Rev-erbα* exacerbates SuHx-induced PAH, and the protective effect of SR9009 is dependent on REV-ERBα. (A) Schematic protocol: *Rev-erbα*$^{+/+}$ and *Rev-erbα*$^{+/-}$ mice were subjected to SuHx and then intraperitoneally injected with SR9009 or an equal volume of vehicle for 3 weeks. (B) Representative RVP images and analysis of RVSP (*n*=7 mice for *Rev-erbα*$^{+/+}$, *n*=8 mice for *Rev-erbα*$^{+/-}$, and *n*=6 mice for *Rev-erbα*$^{+/-}$ +SR9009). The x-axis scale bar indicates 400 ms. (C) Representative images of HE staining and α-SMA immunofluorescence staining, and the quantification of the vascular medial thickness to total vessel size ratios of pulmonary arteries (PAs) (*n*=9 mice for *Rev-erbα*$^{+/+}$, *n*=8 mice for *Rev-erbα*$^{+/-}$, and *n*=7 mice for *Rev-erbα*$^{+/-}$ +SR9009). Scale bar: 50 μm. (D) Echocardiography measurement of PA function and the ratio of pulmonary artery blood flow acceleration time (PAT) to pulmonary artery ejection time (PET) (*n*=9 mice for *Rev-erbα*$^{+/+}$, *n*=8 mice for *Rev-erbα*$^{+/-}$, and *n*=7 mice for *Rev-erbα*$^{+/-}$ +SR9009). (E) Representative images of pulmonary angiography and the quantification of the branch count, total length, and junction count (*n*=4 mice per group). Scale bar: 3 mm. (F) Fulton index [right ventricle weight/ (left ventricle + septum weight), RV/(LV+S)] as a marker of right ventricular (RV) hypertrophy (*n*=9 mice for *Rev-erbα*$^{+/+}$, *n*=8 mice for *Rev-erbα*$^{+/-}$, and *n*=7 mice for *Rev-erbα*$^{+/-}$ +SR9009). (G) Representative images of wheat germ agglutinin (WGA) staining and the quantitative analysis of cardiomyocyte cross-sectional area (*n*=9 mice for *Rev-erbα*$^{+/+}$, *n*=8 mice for *Rev-erbα*$^{+/-}$, and *n*=7 mice for *Rev-erbα*$^{+/-}$ +SR9009). Scale bar: 50 μm. All data are presented as means ± SEM. Statistical significance was determined by two-tailed unpaired Student's *t*-test for E, and one-way ANOVA followed by Tukey's post-hoc test for all other panels. Source data are provided as a Source Data file.

Figure 5. *Rev-erbα* overexpression alleviates SuHx-induced PAH, and VSMC-specific *Rev-erbα* knockout exacerbates PAH. (A-E) WT mice injected with negative control AAV (AAV-NC) or *Rev-erbα* overexpression AAV (AAV-OE-*Rev-erbα*) were subjected to SuHx-induced PAH. (A) Schematic protocol. (B) Representative RVP images and analysis of RVSP (*n*=7 mice per group). The x-axis scale bar indicates 400 ms. (C) Representative images of HE staining and the quantification of the vascular medial thickness to total vessel size ratios of PAs (*n*=7 mice per group). Scale bar: 50 μm. (D) Echocardiography measurement of PA function and the ratio of pulmonary artery blood flow acceleration time (PAT) to pulmonary artery ejection time (PET) (*n*=7 mice per group). (E) Representative images of wheat germ agglutinin (WGA) staining and the quantitative analysis of cardiomyocyte cross-sectional area (*n*=7 mice per group). Scale bars: 200 μm (top) and 50 μm (bottom). (F-K) VSMC-*Rev-erbα*$^{fl/fl}$ and VSMC-*Rev-erbα*$^{-/-}$ mice were subjected to SuHx-induced PAH. (F) Schematic protocol. (G) Representative RVP images and analysis of RVSP (*n*=12 mice

for VSMC-*Rev-erbα*$^{fl/fl}$, *n*=10 mice for VSMC-*Rev-erbα*$^{-/-}$). The x-axis scale bar indicates 400 ms. (H) Representative images of HE staining and the quantification of the vascular medial thickness to total vessel size ratios of PAs (*n*=12 mice for VSMC-*Rev-erbα*$^{fl/fl}$, *n*=11 mice for VSMC-*Rev-erbα*$^{-/-}$). Scale bar: 50 μm. (I) Echocardiography measurement of PA function and the ratio of pulmonary artery blood flow acceleration time (PAT) to pulmonary artery ejection time (PET) (*n*=12 mice for VSMC-*Rev-erbα*$^{fl/fl}$, *n*=10 mice for VSMC-*Rev-erbα*$^{-/-}$). (J) Representative images of pulmonary angiography and the quantification of the branch count, total length, and junction count (*n*=4 mice per group). Scale bar: 3 mm. (K) Representative images of wheat germ agglutinin (WGA) staining and the quantitative analysis of cardiomyocyte cross-sectional area (*n*=12 mice for VSMC-*Rev-erbα*$^{fl/fl}$, *n*=11 mice for VSMC-*Rev-erbα*$^{-/-}$). Scale bars: 200 μm (top) and 50 μm (bottom). All data are presented as means ± SEM. Statistical significance was determined by two-tailed unpaired Student's *t*-test. Source data are provided as a Source Data file.

Figure 6. SR9009 improves mitochondrial homeostasis by mitigating mitophagy in SuHx mice and hypoxic PASMCs. (A-D) WT mice were subjected to normoxia or SuHx and intraperitoneally injected with vehicle or SR9009. (A) Transmission electron microscopy (TEM) shows subcellular structures; red arrows indicate autophagosomes. Scale bars: 2 μm (main) and 500 nm (inset). (B) MitoSOX Red (mitochondrial superoxide, red) and α-smooth muscle actin (α-SMA, green) co-staining in PAs, and the quantification of MitoSOX fluorescence intensity in α-SMA-positive area (*n*=6 mice for normoxia+ Vehicle, *n*=6 mice for normoxia+ SR9009, *n*=9 mice for SuHx+ Vehicle, and *n*=8 mice for SuHx+ SR9009). Scale bars: 30 μm (top) and 60 μm (bottom). (C) Western blot analysis of LC3B and P62 protein expression in mouse lung tissues; GAPDH served as an internal reference (*n*=5 mice for normoxia+ Vehicle, *n*=5 mice for normoxia+ SR9009, *n*=9 mice for SuHx+ Vehicle, and *n*=7 mice for SuHx+ SR9009). (D) Immunofluorescence staining of lung sections for LC3B (Alexa Fluor 647, red) and α-SMA (Alexa Fluor 488, green), and the quantification of LC3B fluorescence intensity in α-SMA-positive vascular smooth muscle cells (*n*=6 mice for normoxia+ Vehicle, *n*=6 mice for normoxia+ SR9009, *n*=10 mice for SuHx+ Vehicle, and *n*=9 mice for SuHx+ SR9009). Scale bars: 30 μm (top) and 60 μm (bottom). (E-I) PASMCs under normoxic or hypoxic conditions were treated with DMSO or SR9009. (E) ROS levels in PASMCs measured by fluorescence microplate reader (excitation: 488 nm, emission: 525 nm) (*n*=6 independent biological replicates). (F) JC-1 staining, indicating mitochondrial membrane potential, and the quantification in PASMCs (*n*=6 independent biological replicates). Scale bar: 100 μm. (G) MitoSOX Red staining (mitochondrial superoxide, red) and the quantification in PASMCs (*n*=3 independent biological replicates). Scale bar: 120 μm. (H) PASMCs are infected with Adv-COX8-mt-Keima and imaged by confocal microscopy to monitor mitophagy (green Ex: 445 nm, red Ex: 561 nm) (*n*=5 independent biological replicates). Scale bars: 70 μm (top) and 140 μm (bottom). (I) Western blot analysis of TOMM20, LC3B, and P62 protein expression in PASMCs; GAPDH served as an internal reference (*n*=6 independent biological replicates). All data are presented as means ± SEM. Statistical significance was determined by two-way ANOVA followed by Tukey's post-hoc test. Source data are provided as a Source Data file.

Figure 7. REV-ERBα regulates mitophagy through transcriptional repression of *Bnip3*. (A-C) PASMCs under normoxic or hypoxic conditions were treated with DMSO or SR9009. (A) Western blot analysis of BNIP3 and BNIP3L protein expression (*n*=6 independent biological replicates). (B) qPCR quantification of *Bnip3* and *Bnip3l* mRNA levels (*n*=5 independent biological replicates for normoxia, *n*=6 for hypoxia, and *n*=5 for hypoxia+SR9009). (C) Representative Co-IP analysis results present the association of LC3B with BNIP3 or BNIP3L in PASMCs. (D) A schematic diagram of the 2 kb *Bnip3* promoter depicts the positions of the putative REV-ERBα binding sites. (E) ChIP assay showed the products amplified from the putative REV-ERBα-binding sites of *Bnip3*. (F) Dual-luciferase reporter assays were used to evaluate luciferase activity of *Bnip3* promoter (*n*=6 independent biological replicates). (G-I) Hypoxic PASMCs were transfected with *Rev-erbα* overexpression plasmid and/or *Bnip3*

overexpression plasmid for 48 h. (G) Representative Ki67 immunofluorescence staining and the quantification of fluorescence density. Nuclei were counterstained with DAPI (*n*=3 independent biological replicates). Scale bars: 100 μm (top) and 200 μm (bottom). (H) Representative EdU incorporation assay images and the quantification of EdU-positive cells (*n*=3 independent biological replicates). Scale bars: 200 μm (top) and 400 μm (bottom). (I) CCK-8 assay to determine the PASMCs viability (*n*=24 independent biological replicates). (J) Graphic abstract of the study (Created with Figdraw, Authorization ID: IRPOI824bc). All data are presented as means ± SEM. Statistical significance was determined by one-way ANOVA followed by Tukey's post-hoc test (for A and B), two-tailed unpaired Student's *t*-test (for F), and two-way ANOVA followed by Tukey's post-hoc test for all other panels. Source data are provided as a Source Data file.

Figure 8. *Bnip3* knockdown alleviates hypoxia-induced PASMC proliferation, and VSMC-specific *Bnip3* overexpression exacerbates SuHx-induced PAH. (A-C) PASMCs were transfected with *Bnip3*-targeting siRNA (*Bnip3* siRNA) or negative control siRNA (NC siRNA), followed by exposure to normoxic or hypoxic conditions. (A) Representative Ki67 immunofluorescence staining and the quantification of fluorescence density. Nuclei were counterstained with DAPI (*n*=6 independent biological replicates). Scale bars: 100 μm (top) and 200 μm (bottom). (B) Representative EdU incorporation assay images and the quantification of EdU-positive cells (*n*=6 independent biological replicates). Scale bars: 200 μm (top) and 400 μm (bottom). (C) CCK-8 assay to determine the PASMCs viability (*n*=20 independent biological replicates). (D-I) WT mice injected with negative control AAV (AAV-NC) or VSMC-specific *Bnip3* overexpression AAV (AAV-OE-*Bnip3*) were subjected to SuHx-induced PAH. (D) Schematic protocol. (E) Fulton index [right ventricle weight/ (left ventricle + septum weight), RV/(LV+S)] as a marker of right ventricular (RV) hypertrophy (*n*=4 mice for normoxia+ AAV-NC, *n*=4 mice for normoxia+ AAV-OE-*Bnip3*, *n*=6 mice for SuHx+ AAV-NC, and *n*=8 mice for SuHx+ AAV-OE-*Bnip3*). (F) Representative RVP images and analysis of RVSP (*n*=4 mice for normoxia+ AAV-NC, *n*=4 mice for normoxia+ AAV-OE-*Bnip3*, *n*=6 mice for SuHx+ AAV-NC, and *n*=8 mice for SuHx+ AAV-OE-*Bnip3*). The x-axis scale bar indicates 400 ms. (G) Representative images of HE staining and the quantification of the vascular medial thickness to total vessel size ratios of PAs (*n*=4 mice for normoxia+ AAV-NC, *n*=4 mice for normoxia+ AAV-OE-*Bnip3*, *n*=6 mice for SuHx+ AAV-NC, and *n*=8 mice for SuHx+ AAV-OE-*Bnip3*). Scale bar: 50 μm. (H) Echocardiography measurement of PA function and the ratio of pulmonary artery blood flow acceleration time (PAT) to pulmonary artery ejection time (PET) (*n*=4 mice for normoxia+ AAV-NC, *n*=4 mice for normoxia+ AAV-OE-*Bnip3*, *n*=6 mice for SuHx+ AAV-NC, and *n*=8 mice for SuHx+ AAV-OE-*Bnip3*). (I) Representative images of wheat germ agglutinin (WGA) staining and the quantitative analysis of cardiomyocyte cross-sectional area (*n*=4 mice for normoxia+ AAV-NC, *n*=4 mice for normoxia+ AAV-OE-*Bnip3*, *n*=6 mice for SuHx+ AAV-NC, and *n*=8 mice for SuHx+ AAV-OE-*Bnip3*). Scale bars: 200 μm (top) and 50 μm (bottom). All data are presented as means ± SEM. Statistical significance was determined by two-way ANOVA followed by Tukey's post-hoc test. Source data are provided as a Source Data file.

Editorial summary:

Pulmonary arterial hypertension (PAH) is a fatal disease involving disrupted metabolic and mitochondrial regulation. Here the authors show that REV-ERBα protects against PAH by repressing BNIP3-driven mitophagy in pulmonary vascular smooth muscle cells, revealing a potential circadian-based therapeutic target.

Peer review information: *Nature Communications* thanks Andrew Bryant, Andrew James, and the other, anonymous, reviewer(s) for their contribution to the peer review of this work. A peer review file is available.

Mice with SuHx treatment

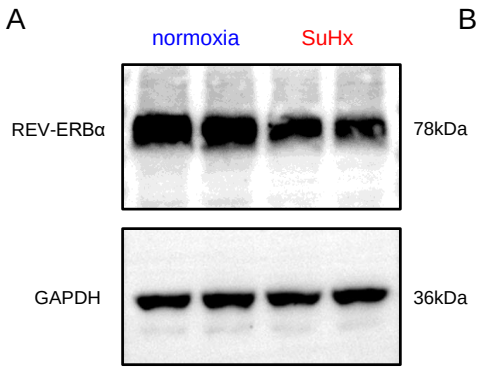

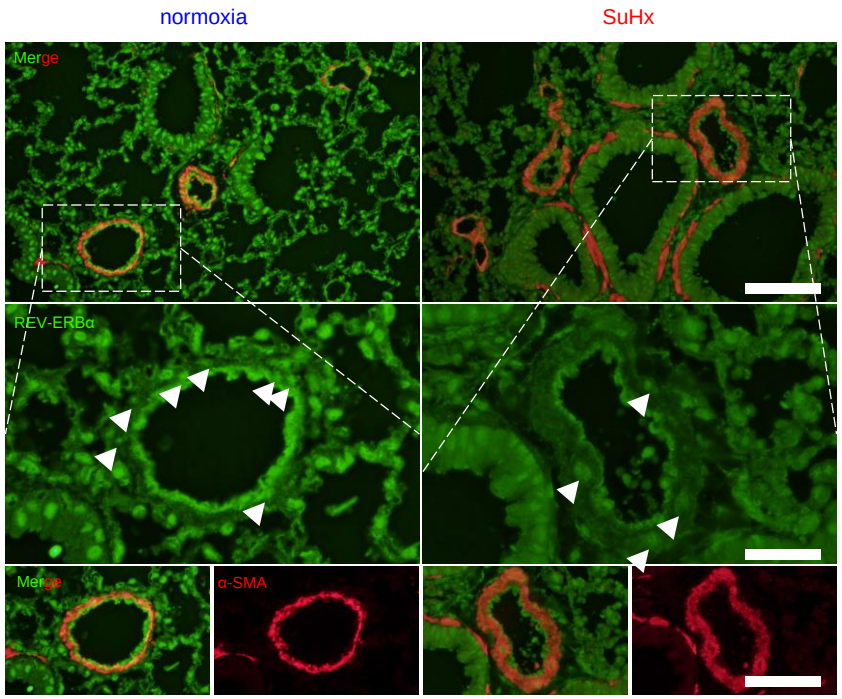

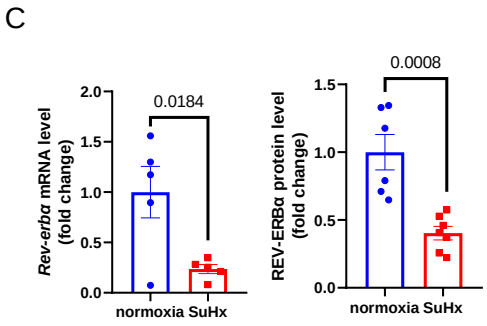

PASMCs with $CoCl_2$ treatment

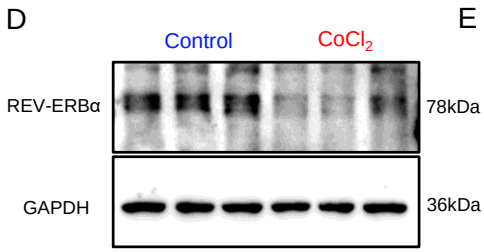

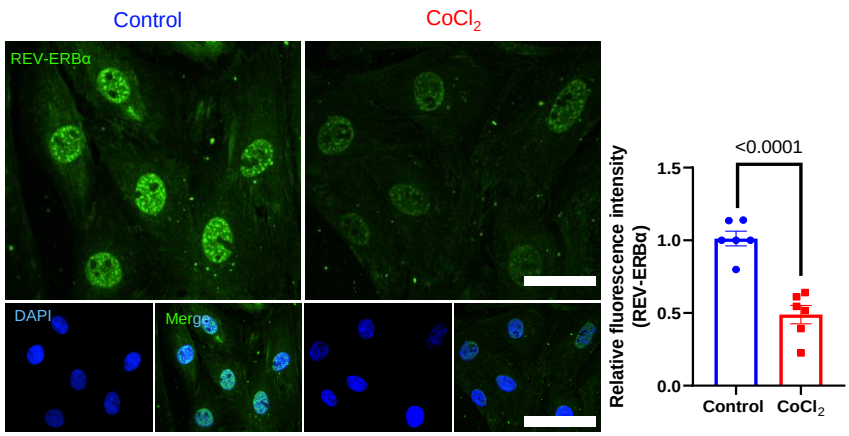

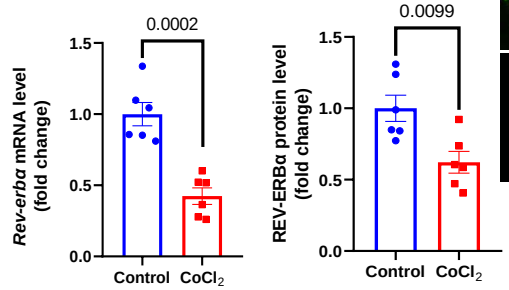

PASMCs with hypoxia treatment

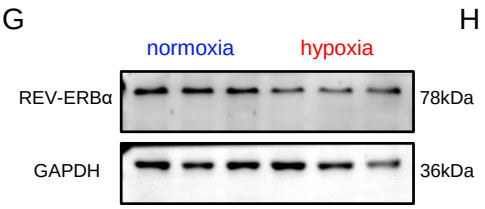

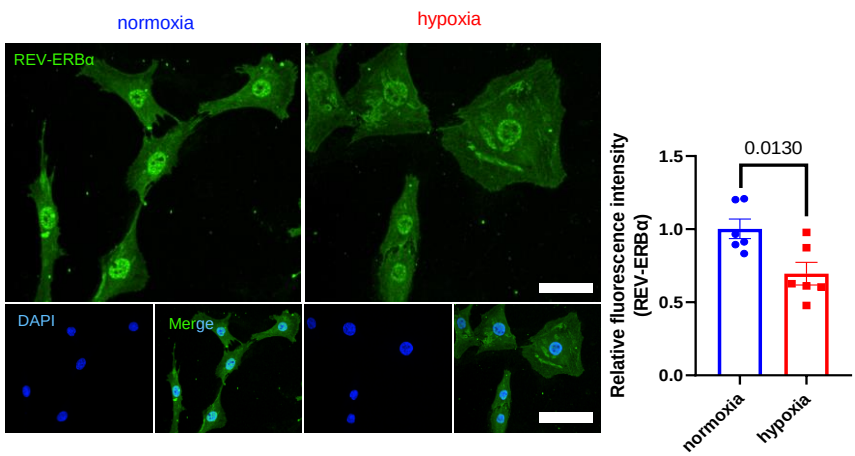

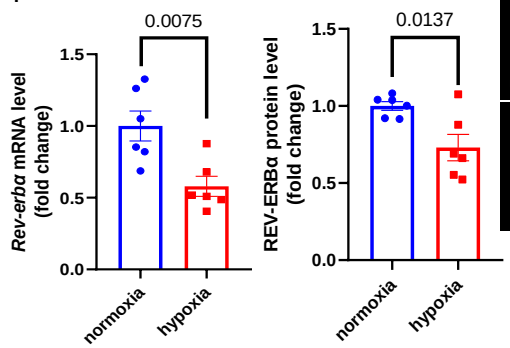

PASMCs with SR9009 treatment

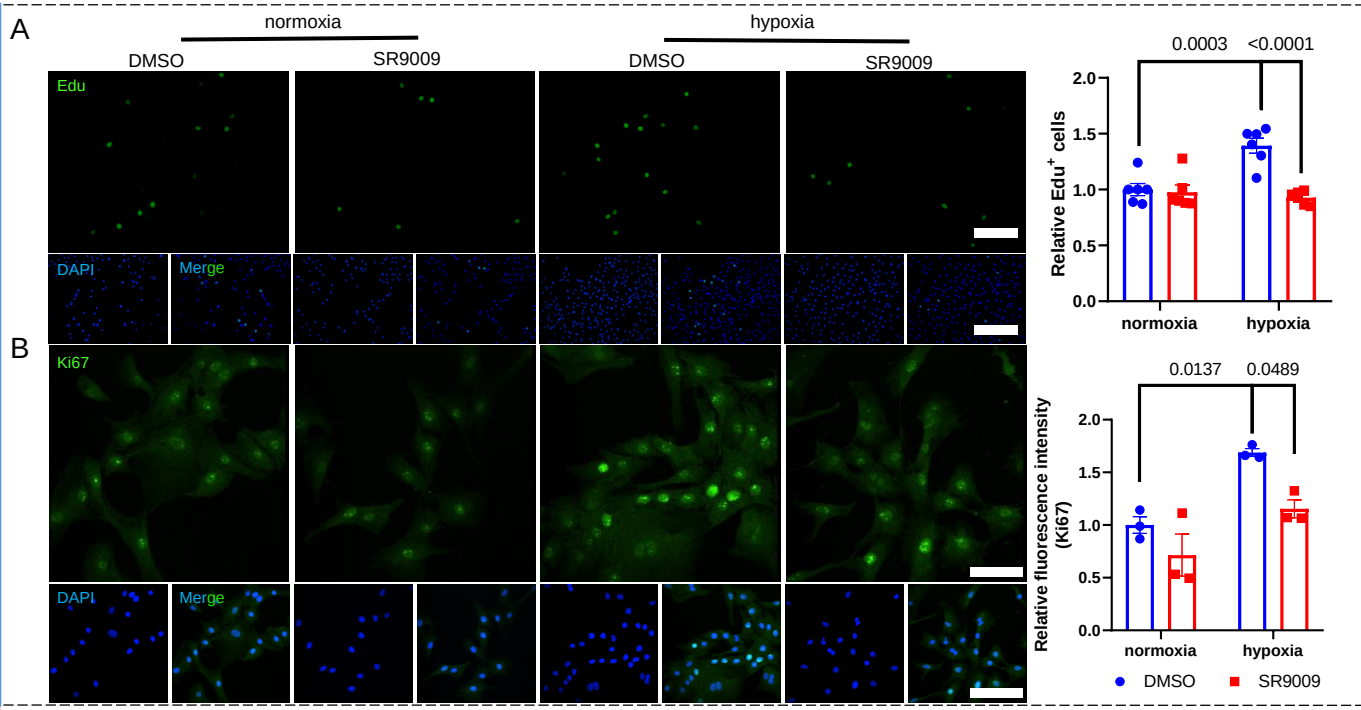

PASMCs with *Rev-erbα* knockdown

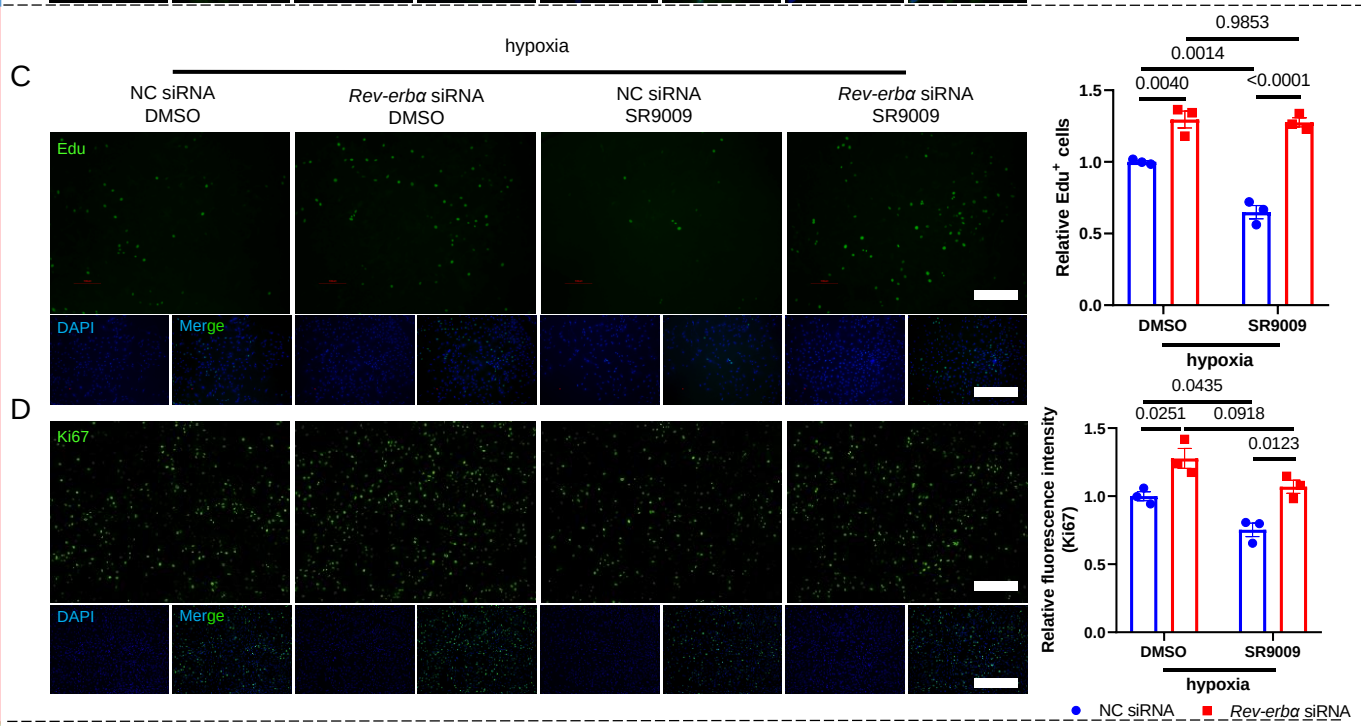

PASMCs with *Rev-erbα* overexpression

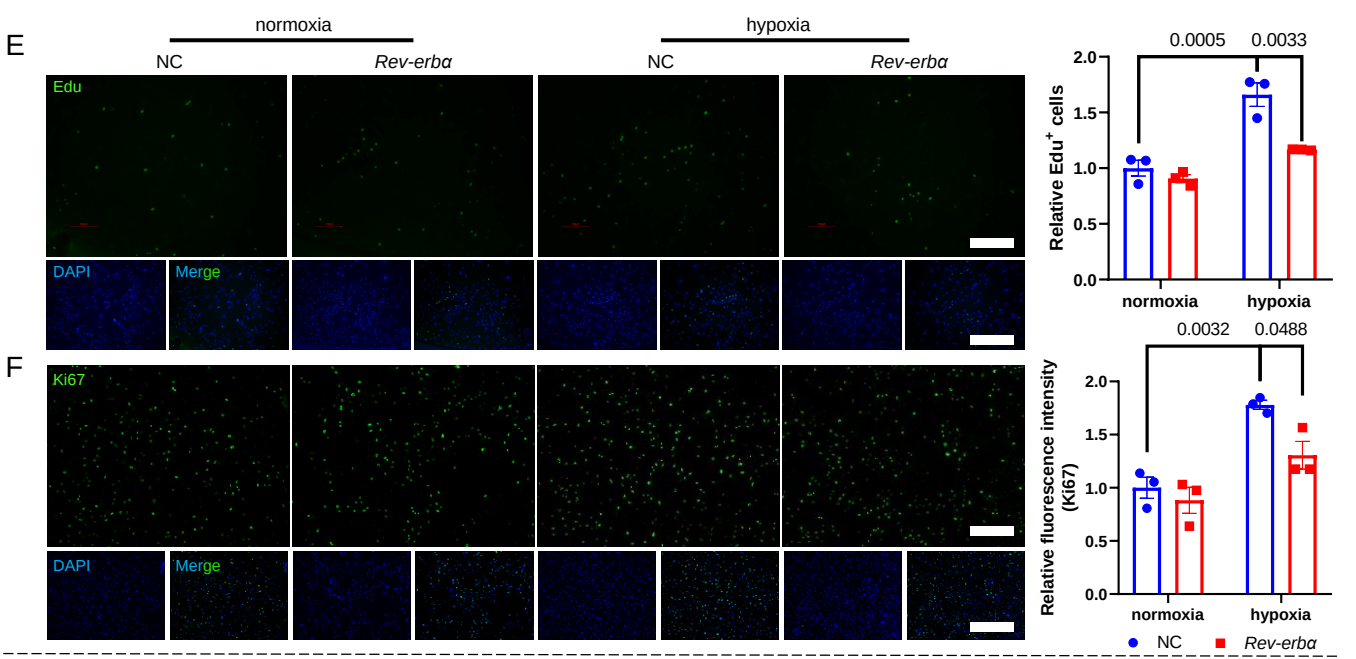

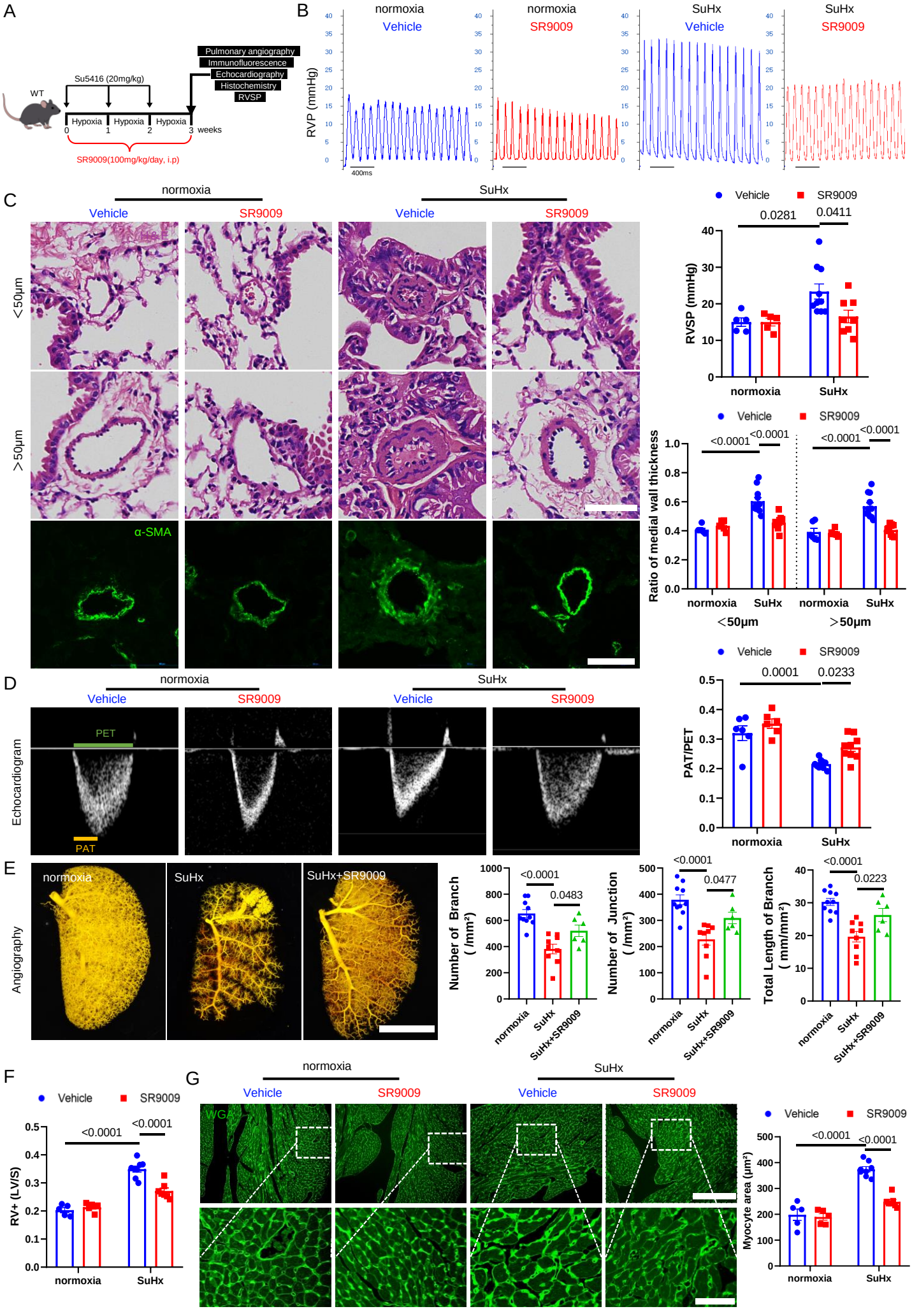
A
WT
Su5416 (20mg/kg)
Hypoxia
Hypoxia
Hypoxia
0
1
2
3 weeks
SR9009(100mg/kg/day, i.p)
Pulmonary angiography
Immunofluorescence
Echocardiography
Histochemistry
RVSP
B
normoxia
Vehicle
normoxia
SR9009
SuHx
Vehicle
SuHx
SR9009
RVP (mmHg)
400ms
C
normoxia
SuHx
Vehicle
SR9009
Vehicle
SR9009
<50μm
>50μm
α-SMA
Vehicle
SR9009
0.0281
0.0411
RVSP (mmHg)
normoxia
SuHx
Vehicle
SR9009
<0.0001
<0.0001
<0.0001
<0.0001
Ratio of medial wall thickness
normoxia
SuHx
normoxia
SuHx
<50μm
>50μm
D
normoxia
SuHx
Vehicle
SR9009
Vehicle
SR9009
Echocardiogram
PET
PAT
Vehicle
SR9009
0.0001
0.0233
PAT/PET
normoxia
SuHx
E
Angiography
normoxia
SuHx
SuHx+SR9009
<0.0001
0.0483
Number of Branch (/mm²)
<0.0001
0.0477
Number of Junction (/mm²)
<0.0001
0.0223
Total Length of Branch (mm/mm²)
normoxia
SuHx
SuHx+SR9009
F
Vehicle
SR9009
<0.0001
<0.0001
RV+ (LV/S)
normoxia
SuHx
G
normoxia
SuHx
Vehicle
SR9009
Vehicle
SR9009
WGA
Vehicle
SR9009
<0.0001
<0.0001
Myocyte area (μm²)
normoxia
SuHx

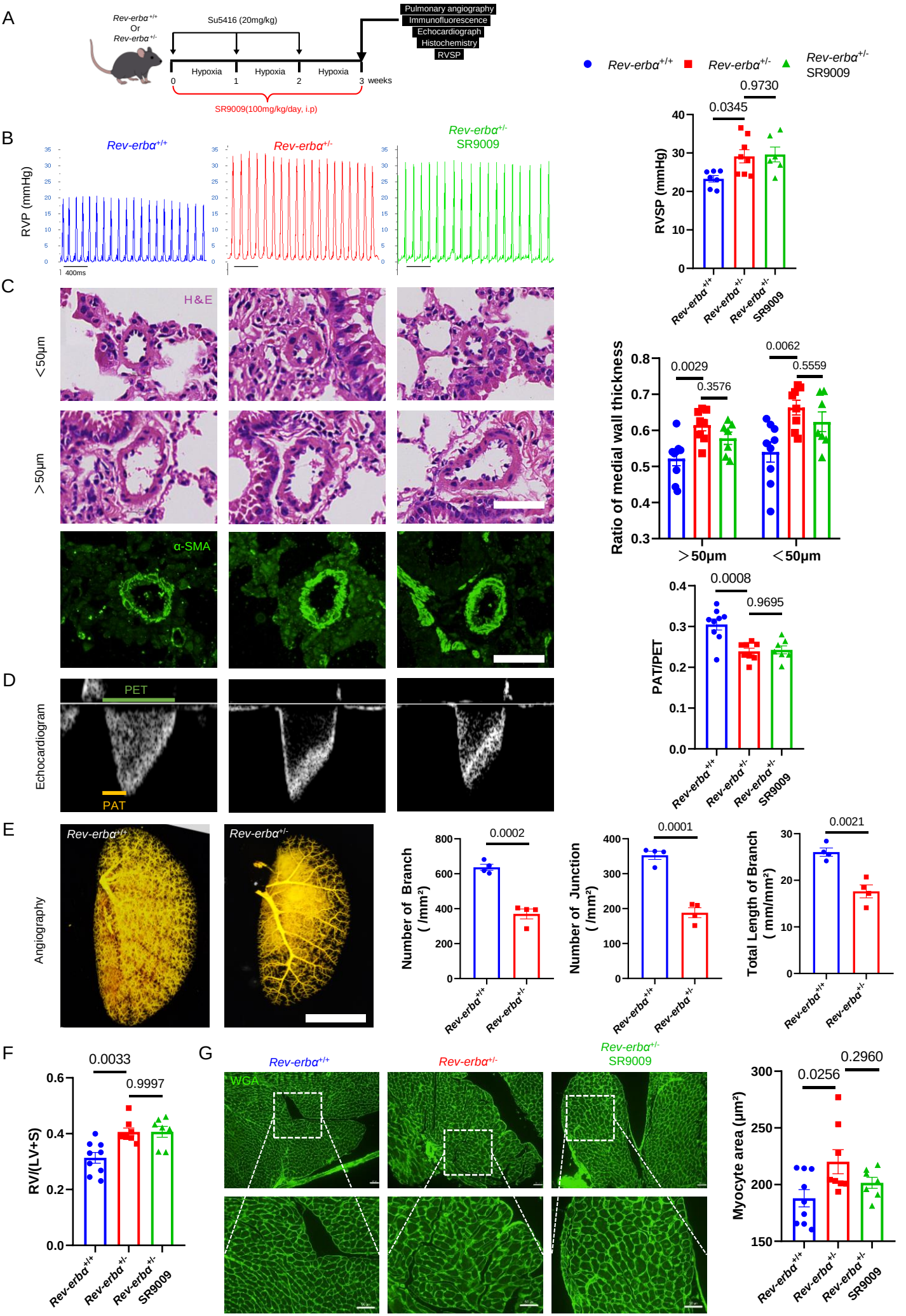
A
Rev-erbα+/+
Or
Rev-erbα+/-
Su5416 (20mg/kg)
Hypoxia
Hypoxia
Hypoxia
0
1
2
3 weeks
SR9009(100mg/kg/day, i.p)
Pulmonary angiography
Immunofluorescence
Echocardiograph
Histochemistry
RVSP
Rev-erbα+/+
Rev-erbα+/-
Rev-erbα+/- SR9009
B
RVP (mmHg)
Rev-erbα+/+
Rev-erbα+/-
Rev-erbα+/- SR9009
400ms
0.9730
0.0345
RVSP (mmHg)
C
H&E
<50μm
>50μm
α-SMA
0.0062
0.0029
0.5559
0.3576
Ratio of medial wall thickness
>50μm
<50μm
0.0008
0.9695
PAT/PET
D
Echocardiogram
PET
PAT
E
Angiography
Rev-erbα+/+
Rev-erbα+/-
0.0002
Number of Branch (/mm²)
0.0001
Number of Junction (/mm²)
0.0021
Total Length of Branch (mm/mm²)
F
0.0033
0.9997
RV/(LV+S)
G
Rev-erbα+/+
Rev-erbα+/-
Rev-erbα+/- SR9009
WGA
0.0256
0.2960
Myocyte area (μm²)

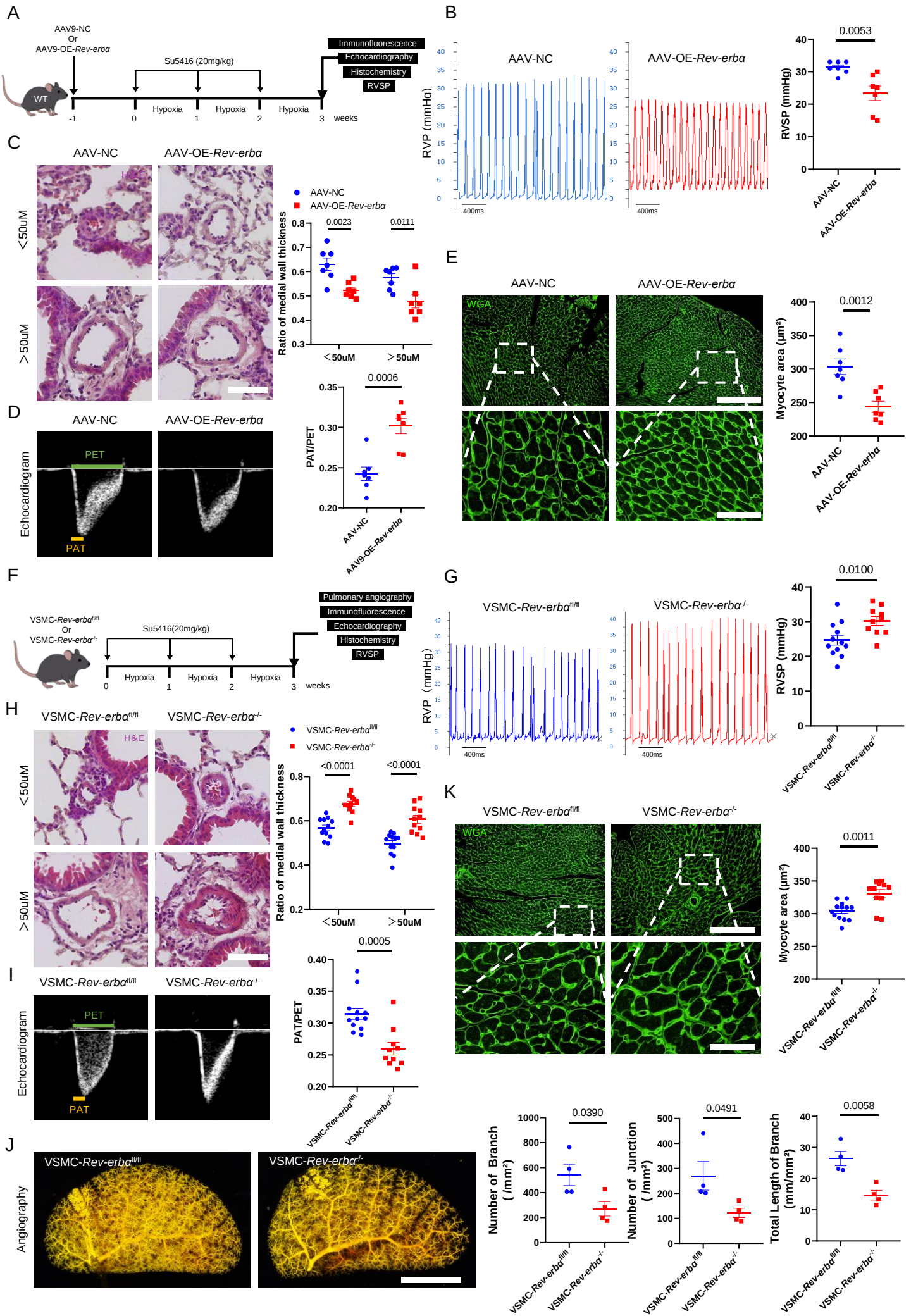
A
AAV9-NC
Or
AAV9-OE-Rev-erbα
Su5416 (20mg/kg)
WT
Immunofluorescence
Echocardiography
Histochemistry
RVSP
Hypoxia
Hypoxia
Hypoxia
-1
0
1
2
3
weeks
B
AAV-NC
AAV-OE-Rev-erbα
RVP (mmHg)
400ms
RVSP (mmHg)
0.0053
C
AAV-NC
AAV-OE-Rev-erbα
H&E
<50uM
>50uM
Ratio of medial wall thickness
0.0023
0.0111
D
Echocardiogram
PET
PAT
PAT/PET
0.0006
E
WGA
Myocyte area (μm²)
0.0012
F
VSMC-Rev-erbα^fl/fl
Or
VSMC-Rev-erbα^-/-
Su5416(20mg/kg)
Pulmonary angiography
Immunofluorescence
Echocardiography
Histochemistry
RVSP
G
VSMC-Rev-erbα^fl/fl
VSMC-Rev-erbα^-/-
RVP (mmHg)
RVSP (mmHg)
0.0100
H
Ratio of medial wall thickness
<0.0001
<0.0001
I
PAT/PET
0.0005
J
Angiography
K
Myocyte area (μm²)
0.0011
Number of Branch (/mm²)
0.0390
Number of Junction (/mm²)
0.0491
Total Length of Branch (mm/mm²)
0.0058

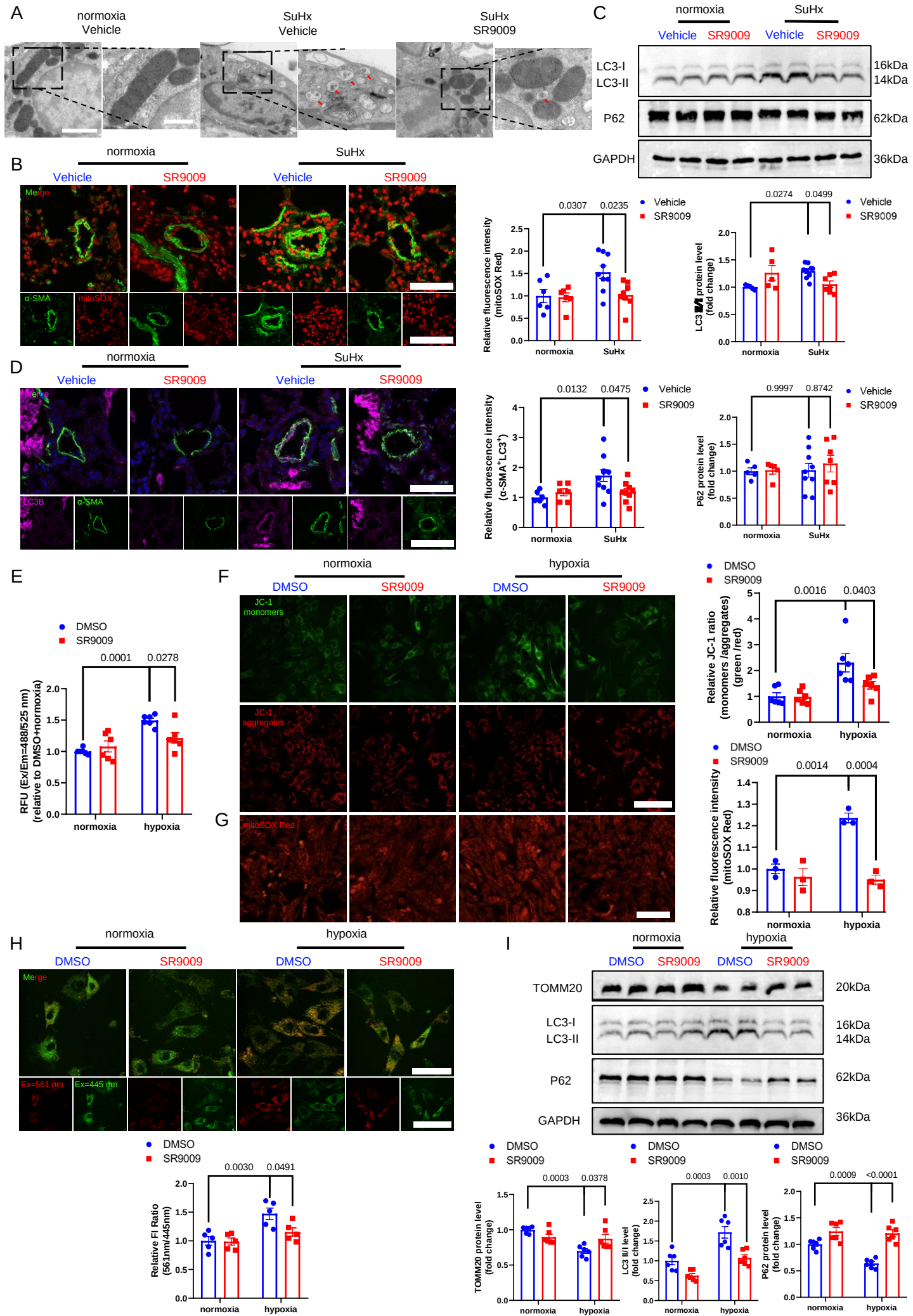
A
normoxia
Vehicle
SuHx
Vehicle
SuHx
SR9009
B
normoxia
SuHx
Vehicle
SR9009
Vehicle
SR9009
Merge
α-SMA
mitoSOX
Relative fluorescence intensity (mitoSOX Red)
0.0307
0.0235
Vehicle
SR9009
normoxia
SuHx
C
normoxia
SuHx
Vehicle
SR9009
Vehicle
SR9009
LC3-I
LC3-II
16kDa
14kDa
P62
62kDa
GAPDH
36kDa
LC3 II/I protein level (fold change)
0.0274
0.0499
P62 protein level (fold change)
0.9997
0.8742
D
normoxia
SuHx
Vehicle
SR9009
Vehicle
SR9009
Merge
LC3B
α-SMA
Relative fluorescence intensity (α-SMA+LC3+)
0.0132
0.0475
E
DMSO
SR9009
0.0001
0.0278
RFU (Ex/Em=488/525 nm) (relative to DMSO+normoxia)
normoxia
hypoxia
F
normoxia
hypoxia
DMSO
SR9009
DMSO
SR9009
JC-1 monomers
JC-1 aggregates
Relative JC-1 ratio (monomers /aggregates) (green /red)
0.0016
0.0403
G
mitoSOX Red
Relative fluorescence intensity (mitoSOX Red)
0.0014
0.0004
H
normoxia
hypoxia
DMSO
SR9009
DMSO
SR9009
Merge
Ex=561 nm
Ex=445 nm
Relative FI Ratio (561nm/445nm)
0.0030
0.0491
I
normoxia
hypoxia
DMSO
SR9009
DMSO
SR9009
TOMM20
20kDa
LC3-I
LC3-II
16kDa
14kDa
P62
62kDa
GAPDH
36kDa
TOMM20 protein level (fold change)
0.0003
0.0378
LC3 II/I level (fold change)
0.0003
0.0010
P62 protein level (fold change)
0.0009
<0.0001

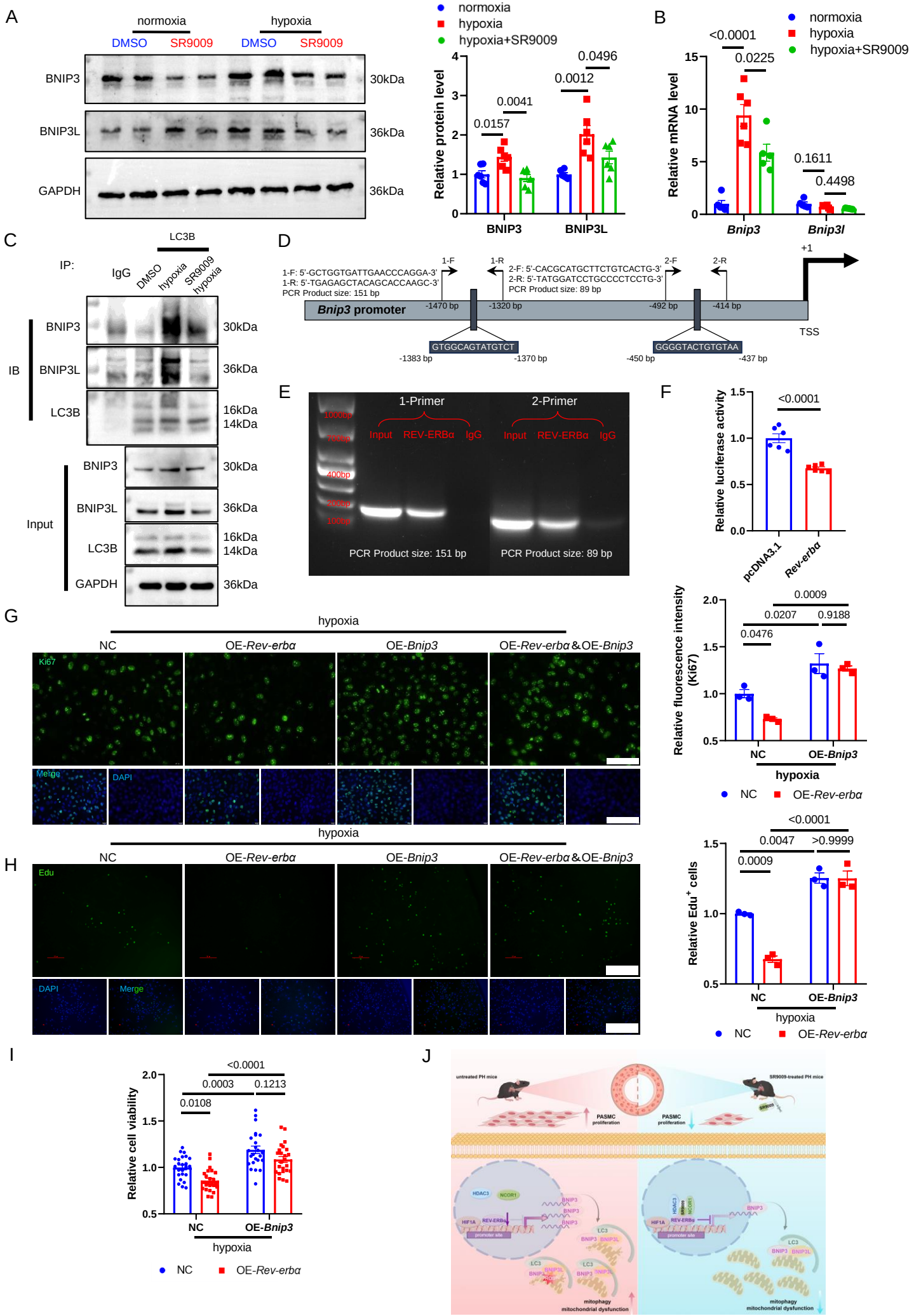
A
normoxia
hypoxia
DMSO
SR9009
DMSO
SR9009
BNIP3
BNIP3L
GAPDH
30kDa
36kDa
36kDa
normoxia
hypoxia
hypoxia+SR9009
Relative protein level
0.0157
0.0041
0.0012
0.0496
BNIP3
BNIP3L
B
normoxia
hypoxia
hypoxia+SR9009
Relative mRNA level
<0.0001
0.0225
0.1611
0.4498
Bnip3
Bnip3l
C
LC3B
IP:
IgG
DMSO
hypoxia
SR9009
hypoxia
IB
Input
BNIP3
BNIP3L
LC3B
GAPDH
30kDa
36kDa
16kDa
14kDa
36kDa
D
1-F: 5'-GCTGGTGATTGAACCCAGGA-3'
1-R: 5'-TGAGAGCTACAGCACCAAGC-3'
PCR Product size: 151 bp
2-F: 5'-CACGCATGCTTCTGTCACTG-3'
2-R: 5'-TATGGATCCTGCCCCTCCTG-3'
PCR Product size: 89 bp
Bnip3 promoter
-1470 bp
-1320 bp
-492 bp
-414 bp
+1
TSS
GTGGCAGTATGTCT
-1383 bp
-1370 bp
GGGGTACTGTGTAA
-450 bp
-437 bp
E
1-Primer
2-Primer
Input
REV-ERBα
IgG
1000bp
700bp
400bp
200bp
100bp
PCR Product size: 151 bp
PCR Product size: 89 bp
F
Relative luciferase activity
<0.0001
pcDNA3.1
Rev-erbα
G
hypoxia
NC
OE-Rev-erbα
OE-Bnip3
OE-Rev-erbα&OE-Bnip3
Ki67
Merge
DAPI
Relative fluorescence intensity (Ki67)
0.0009
0.0207
0.9188
0.0476
NC
OE-Bnip3
hypoxia
NC
OE-Rev-erbα
H
hypoxia
NC
OE-Rev-erbα
OE-Bnip3
OE-Rev-erbα&OE-Bnip3
Edu
DAPI
Merge
Relative Edu+ cells
<0.0001
0.0047
>0.9999
0.0009
NC
OE-Bnip3
hypoxia
NC
OE-Rev-erbα
I
Relative cell viability
<0.0001
0.0003
0.1213
0.0108
NC
OE-Bnip3
hypoxia
NC
OE-Rev-erbα
J
untreated PH mice
SR9009-treated PH mice
PASMC proliferation
PASMC proliferation
HDAC3
NCOR1
HIF1A
REV-ERBα
BNIP3
BNIP3L
LC3
promoter site
mitophagy
mitochondrial dysfunction
mitophagy
mitochondrial dysfunction

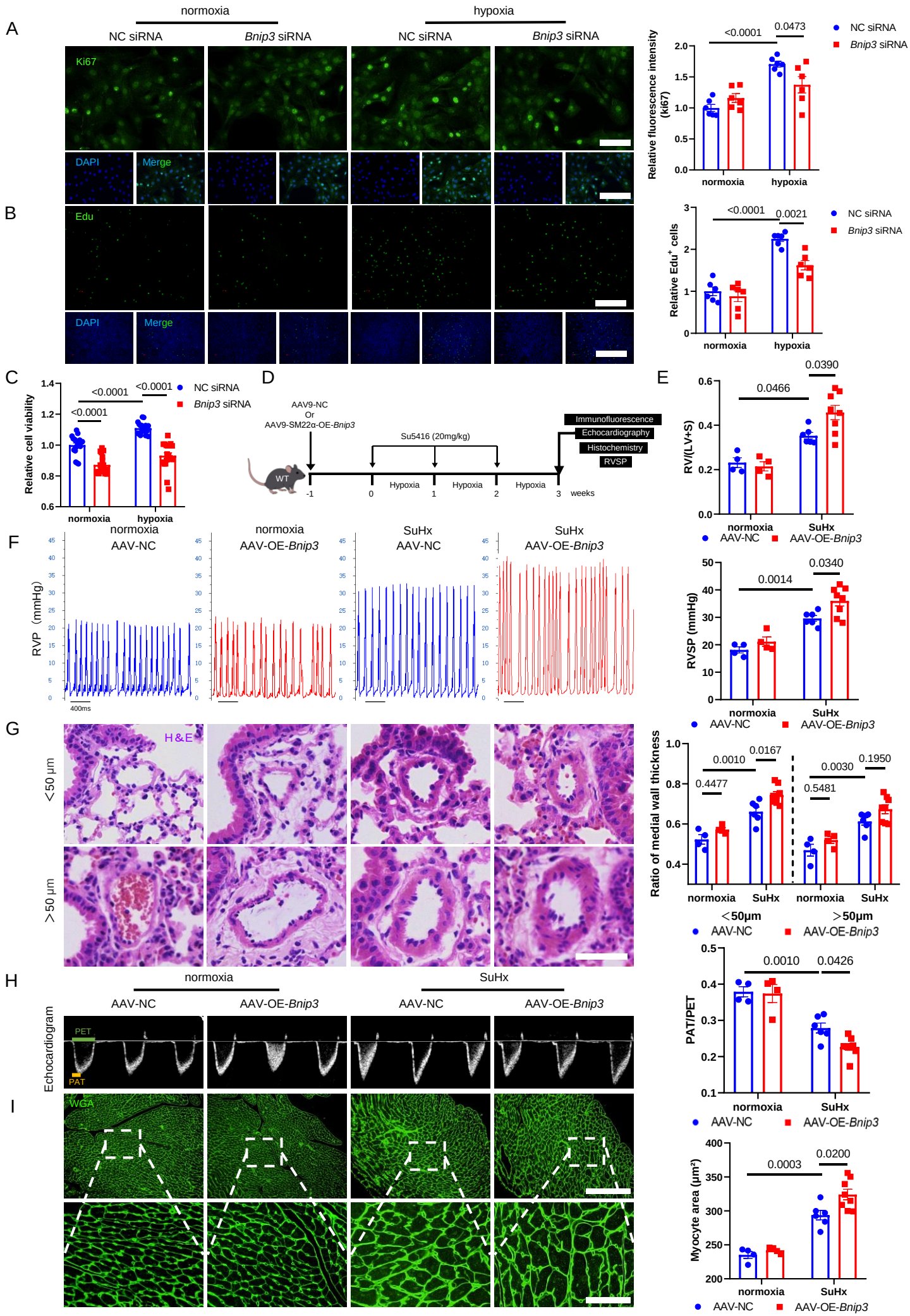
A
normoxia
hypoxia
NC siRNA
Bnip3 siRNA
NC siRNA
Bnip3 siRNA
Ki67
DAPI
Merge
Relative fluorescence intensity (ki67)
<0.0001
0.0473
normoxia
hypoxia
B
Edu
DAPI
Merge
Relative Edu+ cells
<0.0001
0.0021
C
Relative cell viability
<0.0001
<0.0001
<0.0001
D
AAV9-NC
Or
AAV9-SM22α-OE-Bnip3
WT
Su5416 (20mg/kg)
Hypoxia
Hypoxia
Hypoxia
-1
0
1
2
3
weeks
Immunofluorescence
Echocardiography
Histochemistry
RVSP
E
RV/(LV+S)
0.0466
0.0390
AAV-NC
AAV-OE-Bnip3
RVSP (mmHg)
0.0014
0.0340
F
normoxia
AAV-NC
normoxia
AAV-OE-Bnip3
SuHx
AAV-NC
SuHx
AAV-OE-Bnip3
RVP (mmHg)
400ms
G
H&E
<50 μm
>50 μm
Ratio of medial wall thickness
0.4477
0.0010
0.0167
0.5481
0.0030
0.1950
<50μm
>50μm
H
normoxia
SuHx
AAV-NC
AAV-OE-Bnip3
Echocardiogram
PET
PAT
PAT/PET
0.0010
0.0426
I
WGA
Myocyte area (μm²)
0.0003
0.0200